



# **Real-Time Digital Simulation of Inertial Response with Hardware-in-the-Loop Implementation on the CART3 Wind Turbine at the National Wind Technology Center**

Wenzhong Gao and Xiao Wang  
*University of Denver*

Eduard Muljadi, Vahan Gevorgian,  
and Andrew Scholbrock  
*National Renewable Energy Laboratory*

**NREL is a national laboratory of the U.S. Department of Energy  
Office of Energy Efficiency & Renewable Energy  
Operated by the Alliance for Sustainable Energy, LLC**

This report is available at no cost from the National Renewable Energy  
Laboratory (NREL) at [www.nrel.gov/publications](http://www.nrel.gov/publications).

**Technical Report**  
NREL/TP-5D00-68137  
September 2017

Contract No. DE-AC36-08GO28308



# **Real-Time Digital Simulation of Inertial Response with Hardware-in-the-Loop Implementation on the CART3 Wind Turbine at the National Wind Technology Center**

Wenzhong Gao and Xiao Wang  
*University of Denver*

Eduard Muljadi, Vahan Gevorgian, and  
Andrew Scholbrock  
*National Renewable Energy Laboratory*

Prepared under Task No. 065D.1501

**NREL is a national laboratory of the U.S. Department of Energy  
Office of Energy Efficiency & Renewable Energy  
Operated by the Alliance for Sustainable Energy, LLC**

This report is available at no cost from the National Renewable Energy  
Laboratory (NREL) at [www.nrel.gov/publications](http://www.nrel.gov/publications).

National Renewable Energy Laboratory  
15013 Denver West Parkway  
Golden, CO 80401  
303-275-3000 • [www.nrel.gov](http://www.nrel.gov)

**Technical Report**  
NREL/TP-5D00-68137  
September 2017

Contract No. DE-AC36-08GO28308

## NOTICE

This report was prepared as an account of work sponsored by an agency of the United States government. Neither the United States government nor any agency thereof, nor any of their employees, makes any warranty, express or implied, or assumes any legal liability or responsibility for the accuracy, completeness, or usefulness of any information, apparatus, product, or process disclosed, or represents that its use would not infringe privately owned rights. Reference herein to any specific commercial product, process, or service by trade name, trademark, manufacturer, or otherwise does not necessarily constitute or imply its endorsement, recommendation, or favoring by the United States government or any agency thereof. The views and opinions of authors expressed herein do not necessarily state or reflect those of the United States government or any agency thereof.

This report is available at no cost from the National Renewable Energy Laboratory (NREL) at [www.nrel.gov/publications](http://www.nrel.gov/publications).

Available electronically at SciTech Connect <http://www.osti.gov/scitech>

Available for a processing fee to U.S. Department of Energy and its contractors, in paper, from:

U.S. Department of Energy  
Office of Scientific and Technical Information  
P.O. Box 62  
Oak Ridge, TN 37831-0062  
OSTI <http://www.osti.gov>  
Phone: 865.576.8401  
Fax: 865.576.5728  
Email: [reports@osti.gov](mailto:reports@osti.gov)

Available for sale to the public, in paper, from:

U.S. Department of Commerce  
National Technical Information Service  
5301 Shawnee Road  
Alexandria, VA 22312  
NTIS <http://www.ntis.gov>  
Phone: 800.553.6847 or 703.605.6000  
Fax: 703.605.6900  
Email: [orders@ntis.gov](mailto:orders@ntis.gov)

*Cover Photos by Dennis Schroeder: (left to right) NREL 26173, NREL 18302, NREL 19758, NREL 29642, NREL 19795.*

NREL prints on paper that contains recycled content.

## Acknowledgments

This work is part of a National Renewable Energy Laboratory (NREL) Laboratory Directed Research and Development project funded in fiscal year 2015–2016. Additional reports have been published throughout the execution of this program. The authors acknowledge Professor Yongcheol Kang, Moses Kang, and Min Hwang of Chonbuk National University, Republic of Korea; and Lee Jay Fingersh, Paul Fleming, and Rob Wallen of the National Wind Technology Center (NWTC) at NREL for providing technical discussions and support during the development of the Real Time Digital Simulator control and implementation on the Controls Advanced Research Turbine 3 at the NWTC. The authors also acknowledge the input provided by Professor Jun Zhang of the University of Denver as well as Huaiguang Jiang and Blake Lundstrom of NREL’s Power Systems Engineering Center for their thorough technical reviews and suggestions to improve the quality of this report.

## List of Acronyms

AC	Alternating current
AGC	Automatic generation control
CART3	Controls Advanced Research Turbine
CGI	Controllable grid interface
CHIL	Controller hardware-in-the-loop
DC	Direct current
DFIG	Doubly-fed induction generator
DRTS	Digital real-time simulator
FAST	Fatigue, Aerodynamics, Structures, and Turbulence Modeling
FBIC	Frequency-based inertial control
GSC	Generator-side converter
HIL	Hardware-in-the-loop
HUT	Hardware under test
LSC	Line-side converter
MPPT	Maximum power point tracking
NREL	National Renewable Energy Laboratory
NWTC	National Wind Technology Center
p.u.	Per unit
PCC	Point of common coupling
PHIL	Power hardware-in-the-loop
PMSG	Permanent magnet synchronous generator
ROCOF	Rate of change of frequency
RTDS	Real Time Digital Simulator
SAIC	Stable adaptive inertial control
SCADA	Supervisory control and data acquisition
SIC	Stepwise inertial control
TLIC	Torque-limit-based inertial control
TSR	Tip-speed ratio
WPP	Wind power plant
WTG	Wind turbine generator

## Executive Summary

With increasing penetrations of wind power on electric grids, the stability and reliability of interconnected power systems might be impacted. In some countries that have developed renewable energy sources and systems, grid codes have been revised to require wind power plants (WPPs) to provide ancillary services to support power system frequency in case of severe grid events. To do this, wind turbine generators (WTGs) should be deloaded to reserve a certain amount of active power for primary frequency response; however, deloading curtails annual energy production, and the market for this type of service is not widely available and needs to be further developed.

In this report, we focus on the temporary frequency support provided by WTGs through inertial response. WTGs have the potential to provide inertial response, but appropriate control methods should be implemented. With the implemented inertial control methods, wind turbines are capable of increasing their active power output by releasing some of their stored kinetic energy when a frequency excursion occurs. Active power can be temporarily boosted beyond the maximum power points, after which the rotor speed decelerates, and subsequently an active power output reduction restores the kinetic energy.

In this report, we develop two types of models for wind power systems: the first is common, based on the wind power aerodynamic equation, and the power coefficient can be regressed using nonlinear functions; the second is much more complicated, wherein the wind turbine system is modeled using the Fatigue, Aerodynamics, Structures, and Turbulence Modeling (FAST) tool with several degrees of freedom. In this work, we use the aggregated WPP connected to a nine-bus test power system, modeled in both MATLAB/Simulink and a digital real-time simulator (DRTS). We implement two distinct types of inertial control methods in the modeled wind turbines: frequency-based inertial control (FBIC) and stepwise inertial control. We compare the performances of the two methods in terms of their frequency nadirs, rates of change of frequency, and recovery times. We conclude the results under various wind speeds and penetration cases, which provide insight into designing the inertial response of WTGs. Further, we discuss the impact of the parameters on the performance of the inertial control methods. We evaluate the scaling factors for the FBIC method and the slope values for the torque-limit-based inertial control (TLIC) methods. The simulation work shows the characteristics of different inertial responses compared to conventional synchronous generators. Based on the simulation results, we modify, improve, and test the inertial control methods under a more realistic wind turbine model based on FAST. We then validate the inertial responses under highly turbulent wind conditions generated by TurbSim, and we examine their influences on the turbine mechanical components. The extensive simulation proves the effectiveness of the proposed inertial control methods as well as the nine-bus test power system network we used.

We then reconsider the parameters. We rebuild the same test power system using Real Time Simulator Computer-Aided Design, and we implement the inertial control methods in the real Controls Advanced Research Turbine 3 (CART3), which is prepared for the hardware-in-the-loop field-test simulation. After the configuration for the hardware and software hybrid simulation platform are complete, the inertial response is further tested on a real wind turbine for the first time, in which CART3 outputs a controlled inertial response against the emulated frequency excursion, provided by the real-time simulated power system test bed in the DRTS.

This work builds an advanced simulation platform to evaluate the controlled inertial response from WTGs. The obtained simulation results generally indicate that improved power system frequency reliability can be achieved with controlled inertial response from wind turbines. The two implemented inertial control methods present different features with respect to the turbine operation and the frequency transient of the interconnected power system, such that the TLIC method leads to more powerful grid frequency support compared to that of the FBIC method; however, the probability of experiencing a secondary frequency dip should be considered because the TLIC power reference is set independent of the measured grid frequency. The mechanical loading analysis presented shows that the inertial response might decrease thrust-related turbine loadings (e.g., blade flapwise bending and tower fore-aft bending) while increasing the loadings on the shaft connecting the rotor low-speed side and high-speed shaft.

# Table of Contents

<b>1</b>	<b>Introduction</b> .....	<b>1</b>
<b>2</b>	<b>Modeling and Controlling a Variable-Speed Wind Turbine Generator</b> .....	<b>4</b>
2.1	Variable-Speed Wind Turbine Generators.....	4
2.2	Basic Control Concepts for Variable-Speed Wind Turbines.....	4
2.3	Power Converter Control Topology for a Permanent Magnet Synchronous Generator-Wind Turbine Generator.....	5
2.4	FAST-Based CART3 Model.....	6
<b>3</b>	<b>Inertial Control Methods for Variable-Speed Wind Turbine Generators</b> .....	<b>8</b>
3.1	Frequency-Based Inertial Control.....	8
3.2	Stepwise Inertial Control.....	8
3.3	Comparison of Frequency-Based Inertial Control to Stable Adaptive Inertial Control.....	10
3.4	Modification to the Torque-Limit-Based Inertial Control Method Considering Turbulent Wind Conditions.....	11
<b>4</b>	<b>Modified Western Electricity Coordinating Council Three-Machine, Nine-Bus Test Electric Grid</b>	<b>12</b>
4.1	Scenario 1: SG3 Is Modified at Bus 3.....	12
4.2	Scenario 2: SG4 Is Connected to Bus 7.....	12
<b>5</b>	<b>Case Studies</b> .....	<b>14</b>
5.1	Comparison of Frequency-Based Inertial Control to Stable Adaptive Inertial Control in the Simulated Power System.....	14
5.2	Impact of Scaling Factors on the Performance of Frequency-Based Inertial Control Method ...	17
5.3	Impact of Slope Values on the Performance of the Torque-Limit-Based Inertial Control Method	19
5.4	Assessment of Inertial Response Under Highly Turbulent Wind Conditions.....	21
<b>6</b>	<b>Field-Testing Using Hardware-in-the-loop Techniques</b> .....	<b>26</b>
<b>7</b>	<b>Conclusions</b> .....	<b>33</b>
	<b>References</b> .....	<b>34</b>

## List of Figures

Figure 1. Topology of a PMSG-WTG .....	5
Figure 2. Layout of the CART3 model using FAST and TurbSim.....	6
Figure 3. Simplified interface between CART3 and the connected power system.....	7
Figure 4. Simplified interface between CART3 and the connected power system.....	8
Figure 5. SAIC scheme in the rotor speed plane.....	9
Figure 6. Scheme of TLIC in the rotor speed plane.....	9
Figure 7. Comparison of the typical SIC method to the SAIC method .....	10
Figure 8. Comparison of SAIC to FBIC .....	10
Figure 9. Control logic of accelerating the wind turbine in the modified TLIC method .....	11
Figure 10. Modified nine-bus power system—Scenario 1.....	12
Figure 11. Modified nine-bus power system—Scenario 2.....	13
Figure 12. Results for 9.52% penetration under low wind speed .....	15
Figure 13. Results for 9.52% penetration under high wind speed .....	15
Figure 14. Results for 30.9% penetration under low wind speed .....	16
Figure 15. Results for 30.9% penetration under high wind speed .....	16
Figure 16. Frequency nadir with respect to different scaling factors.....	17
Figure 17. ROCOF with respect to different scaling factors .....	18
Figure 18. Recovery time with respect to different scaling factors .....	18
Figure 19. Illustration of different slope values in the TLIC method .....	19
Figure 20. Frequency profile and power-speed characteristics when the wind speed is 8.2 m/s.....	20
Figure 21. Frequency profile and power-speed characteristics when the wind speed is 9 m/s.....	20
Figure 22. Frequency profile and power-speed characteristics when wind speed is 10 m/s.....	21
Figure 23. Diagram of AGC .....	22
Figure 24. Inertial response of CART3 under turbulent wind intensity 5% .....	23
Figure 25. Inertial response of CART3 under turbulent wind intensity 10% .....	23
Figure 26. Illustration of the loads on the wind turbine mechanical components .....	24
Figure 27. Impact of inertial control methods on the wind turbine components .....	25
Figure 28. NREL’s CART3 (left) and CART2 (right). <i>Photo by L.J. Fingersh, NREL 19937</i> .....	27
Figure 29. FAST-based CART3 model in Simulink.....	28
Figure 30. User interface of the CART3 SCADA system .....	28
Figure 31. Configuration of the CHIL test system.....	29
Figure 32. CART3 inertial response with FBIC method—Scenario 1 and Scenario 2.....	30
Figure 33. CART3 inertial response with TLIC method—Scenario 1 and Scenario 2.....	31
Figure 34. Configuration of the PHIL simulation with the General Electric wind turbine.....	32

## List of Tables

Table 1. Scenarios for the Case Studies with Different Wind Power Penetration Levels and Wind Speeds	14
--	----

# 1 Introduction

Wind energy has experienced significant growth in recent decades, and in some areas of the world the penetration level of wind power on electric grids attains 50% [1]. To deliver alternating current (AC) power to the grid directly, a fixed-speed wind turbine generator (WTG) is equipped with a full-span pitch control system that synchronizes the rotor speed to the grid frequency; however, the overall aerodynamic efficiency of fixed-speed WTGs is relatively low, and the turbines suffer severe fatigue damage from load spikes during wind gusts [2]. The application of affordable power electronics and advances in modern WTG control enable sophisticated wind turbine design with variable operation. This improves the aerodynamic efficiency and the electromechanical compliance by leveraging the inertia of the variable-speed rotating blade to buffer the mechanical stresses from the wind turbulence and keep them from directly impacting the gearbox and other mechanical components in the conversion path of transferring energy from wind to the electric grid.

A wind turbine is operated in variable-speed mode because the extracted mechanical (aerodynamic) power can be maximized by maintaining the optimal tip-speed ratio (TSR). The majority of wind turbines installed in modern wind power plants (WPPs) are variable-speed WTGs, which typically employ doubly-fed induction generators (DFIGs) and permanent magnet synchronous generators (PMSGs). It is proven that on average a variable-speed WTG will collect up to 10% more annual energy than a fixed-speed WTG that has the same capacity [2]. The increased energy capture might be easily offset by the cost of power converters, but variable-speed WTGs can essentially improve the injected power quality into the grid. In addition, the variable-speed operation reduces the structural loads on the turbine's mechanical components; thus, variable-speed WTGs are expected to have a longer life span.

Difficulties arise when integrating large-scale WPPs into the electric grid. Frequency stability is a primary concern of transmission system operators. Conventional synchronous generators can provide inertial response—i.e., the release of the kinetic energy stored in their rotating masses—during a frequency dip due to sudden imbalances between demand and generation. The inertial response from the generator occurs in the first few seconds of a frequency event, such as a trip of a synchronous generator or a loss of a transmission line. This inertial response from synchronous generators restricts the rate of change of frequency (ROCOF). After the inertial response, the primary frequency response increases the active power output of the available synchronous generators (based on droop control), so the frequency nadir is maintained above the secure level; otherwise, underfrequency load-shedding relays and generation protection relays might be triggered, which can result in a cascading blackout in a power system [3]. Secondary frequency control, also known as automatic generation control (AGC), assigns the power set point of each synchronous generator, and the frequency will recover to the nominal value. Variable-speed wind turbines are equipped with power converters that enable them to be partially or completely decoupled from the electric power system. Although wind energy conversion systems can be operated to some extent independent of electric power system disturbances, the frequency stability of the power system is deteriorated because of the decreased inertial and primary frequency response caused by the large-scale integration of the variable-speed WTGs. The ability to resist frequency deviation is reduced when the rotating kinetic energy of the conventional power plants is reduced as the retired plants are replaced with large deployments of wind power generation.

Transmission system operators revise their grid codes to accommodate increases in wind power integration. Large WPPs in North America are required to provide frequency support similar to that from the inertial response of synchronous generators [4]. Variable-speed WTGs are capable of releasing kinetic energy; in fact, the rotor speed range of a variable-speed WTG is quite large (30%–60%). Further, the released inertial power can be designed with flexible control methods, so the frequency support effect might be sustained for up to 10 seconds. The inertial response of variable-speed WTGs contributes to improving the frequency nadir and restricting the ROCOF to enhance the stability of a power system.

Various inertial control methods have been developed to achieve synthetic inertial response. These can be categorized into two types: (1) frequency-based inertial control (FBIC), in which the rotor speed is regulated according to the ROCOF (or frequency deviation) in a manner that is similar to that of synchronous generators [5], [6]; and (2) stepwise inertial control (SIC), in which a variable-speed WTG is controlled to release constant active power for a limited time [7], [8], with the preprogrammed power reference designed in the power-speed plane. An improved FBIC method was proposed in [9] in which the gains for the ROCOF term and droop term are adaptive to the predisturbance stored kinetic energy, and the proposed control method was verified in a modeled WPP simulated by considering the wake effect. The authors of [10], [11] proposed improved SIC methods with the goal of avoiding the second frequency dip and overdeceleration experienced in a system controlled by classic SIC methods.

Most of the literature verifies the WTG inertial response under the assumption of a constant wind speed; however, in reality, wind speed might vary significantly when the inertial response lasts for tens of seconds. In this context, we propose an improved SIC method based on the control strategy in [10] and make it work under highly turbulent wind conditions. The modified SIC is compared to the FBIC method under different wind power penetration levels and wind conditions, and it is simulated in a Western Electricity Coordinating Council nine-bus electric grid using MATLAB/Simulink. The wind turbine is modeled using the Fatigue, Aerodynamics, Structures, and Turbulence Modeling (FAST) program [12]; and the mechanical parameters used are taken from the Controlled Advanced Research Turbine 3 (CART3), which is a real wind turbine located at the National Wind Technology Center (NWTC) of the National Renewable Energy Laboratory (NREL). The stochastic turbulent wind speed is generated by TurbSim [13] with tunable turbulence intensity factors. The inertial control methods are completely evaluated from both the electrical and mechanical aspects, which are obtained using advanced simulation tools developed by NREL.

Further, the frequency support provided by variable-speed WTGs is verified in the field test with hardware-in-the-loop (HIL) scenarios. This testing scheme combines real hardware with the real-time dynamics of the simulated components, which provides a more effective and reliable test bed to evaluate the prototype [14]. In the first step, we modify the basic control concepts for CART3 and implement the inertial control methods in the wind turbine supervisory control and data acquisition system (SCADA) system. The test power system—the Western Electricity Coordinating Council nine-bus electric grid—is remodeled in the Real Time Digital Simulator (RTDS) to provide frequency dynamics at the point of common coupling (PCC). In the second step, the aforementioned HIL test is extended to a complete power-hardware-in-the-loop (PHIL) simulation. The controllable grid interface (CGI) functions as a power amplifier that is capable of sinking and sourcing power. CART3, with the implemented inertial control methods, is

connected to the CGI bus and reacts to the real frequency excursion at the PCC. The CART3 electric variables are collected and sent back to the RTDS to complete the closed-loop structure. By using the developed test platform, the response of the wind turbine can be effectively evaluated. The CGI is controlled to provide the designated grid-side conditions and faults without causing disturbances to the main grid.

## 2 Modeling and Controlling a Variable-Speed Wind Turbine Generator

### 2.1 Variable-Speed Wind Turbine Generators

Typical variable-speed WTGs are referred to as DFIGs or PMSGs, which are defined as Type 3 and Type 4 wind energy conversion systems, respectively [15]. The capacity of the power converter can be sized to process the slip power of the DFIG, thus it is the partial power of the WTG's capacity (e.g., 30% to operate the DFIG within  $\pm 30\%$  slip). Type 4 WTGs consist of a full converter system interconnecting a PMSG's stator circuits to the PCC. Compared to DFIG-WTGs, PMSG-WTGs are completely decoupled from the grid, and a direct-drive PMSG-WTG can be driven directly by the wind turbines because of their multipole structures; therefore, the gearbox, which is regarded as a vulnerable part that can be expensive to fix, can be removed. These features lead to higher efficiency and reliability of PMSG-WTGs; however, the cost of PMSG-WTGs is expected to be higher because of their full converters, and the size of their direct-drive systems is larger because of their multipole structures. Even so, the market share of PMSG-WTGs is increasing following the reduced price of power electronics, especially in the offshore wind market.

### 2.2 Basic Control Concepts for Variable-Speed Wind Turbines

Two control units work together in a variable-speed WTG. A pitch controller regulates the pitch angle to restrict the rotor speed or mechanical power when the wind speed is above the rated value, which is also necessary to reduce the loads on the mechanical components of a wind turbine. The rotor speed below the rated value is controlled by the power converter system, which is also in charge of the power injection of a WTG. The rotor speed is regulated to maintain the optimal TSR to maximize the mechanical power extraction from the wind. The mechanical power is formulated in (1) [16] as:

$$P_m = \frac{1}{2} \rho \pi R^2 V_w^3 C_p(\lambda, \beta) \quad (1)$$

The available mechanical power relates to the power coefficient,  $C_p$ . It is determined by the TSR,  $\lambda$ , only when the pitch angle,  $\beta$ , is held constant. The TSR is defined as:

$$\lambda = \frac{\omega_r R}{V_w} \quad (2)$$

A generic method using nonlinear functions to model  $C_p$  can be found in [17]. The maximum power coefficient,  $C_{p,max}$ , corresponds to the optimal TSR and optimal pitch angle. Obviously, the rotor speed should be regulated proportionally to the wind speed to maximize the power extraction. In one of the control topologies, the electromagnetic torque commands were calculated to maintain the optimal rotor speed according to the wind speed measurement, and the pitch controller maintained the extracted mechanical power at the rated value when the wind speed was above the rated value; however, tracking the optimal rotor speed tightly resulted in severe torque transients, and the injected power oscillated a lot due to the wind turbulence. In addition, it is difficult to measure the wind speed accurately at the point of the blade tips. As a result, it is more common to calculate the electromagnetic power or torque directly according to

a predesigned lookup table. Because the optimal TSR,  $\lambda_{opt}$ , and  $C_{p,max}$  are known in advance, the electromagnetic power reference is deduced as:

$$P_e = K \omega_r^3 \quad (3)$$

where:

$$K = \frac{1}{2} \rho \pi R^5 \frac{C_{p,max}}{\lambda_{opt}^3} \quad (4)$$

The WTG operates under maximum power point tracking (MPPT) mode, with the power converter regulating the power according to the reference, which is updated in cubic relation to the rotor speed. In this method, the inertia of the wind turbine's rotating mass acts as an inductance in the electric circuit: it absorbs the torque fluctuations caused by the wind turbulence. The power fluctuations caused by the wind turbulence are smoothed out and absorbed as kinetic energy instead of being delivered directly to the grid; thus, the power quality of the grid is improved [18]. The pitch controller is used to restrict the rotor speed from exceeding the rated speed in this control topology. Only power and rotor speed sensors are required to achieve MPPT control in this method. Thus, the rotor speed and the torque are independently controlled.

### 2.3 Power Converter Control Topology for a Permanent Magnet Synchronous Generator-Wind Turbine Generator

According to the commonly used control concept, the entire structure of a PMSG-WTG is shown in Figure 1. The generated power is injected to the grid through the fully-rated power converters.

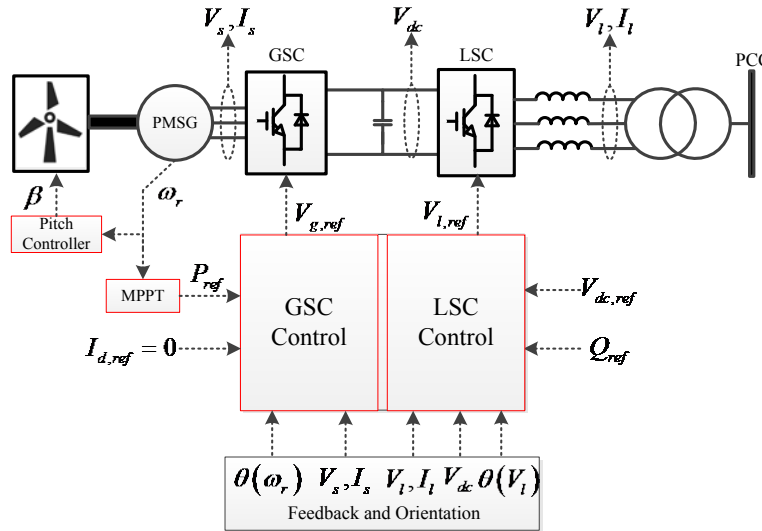


Figure 1. Topology of a PMSG-WTG

The generator-side converter (GSC) employs the zero d-axis current control, and the electromagnetic torque is determined by the q-axis current only when the rotating coordinate is aligned to the permanent flux of a PMSG. Voltage-oriented control is applied at the line-side

converter (LSC), combining the feed-forward structure to achieve the decoupled active and reactive power control. The conservation of energy within the direct current (DC) bus dictates that the real power generated by the GSC ( $P_{GSC}$ ) must be transferred directly to the LSC ( $P_{LSC}$ ), or  $P_{GSC} = P_{LSC}$ . Otherwise, if  $P_{GSC} > P_{LSC}$ , the DC bus voltage will increase; or if  $P_{GSC} < P_{LSC}$ , the DC bus voltage will decrease. As a result, the active power control of the LSC is often substituted by controlling the constant DC-link voltage. Detailed control instructions can be found in [16].

## 2.4 FAST-Based CART3 Model

CART3 is a 600-kW three-bladed turbine located at the NWTC, in Boulder, Colorado. This machine is especially designed for testing advanced control concepts with a customized and reprogramming real-time controller and numerous sensors for monitoring performance [19]. CART3 employs a Type 4 WTG with a full converter system. Each blade can be independently pitched through its own servo system. To research the characteristics of CART3 before the field test, NREL engineers developed a detailed CART3 model based on the FAST program in MATLAB/Simulink. As illustrated in Figure 2, the CART3 model incorporates a simplified generator model, yaw controller, and pitch controller.

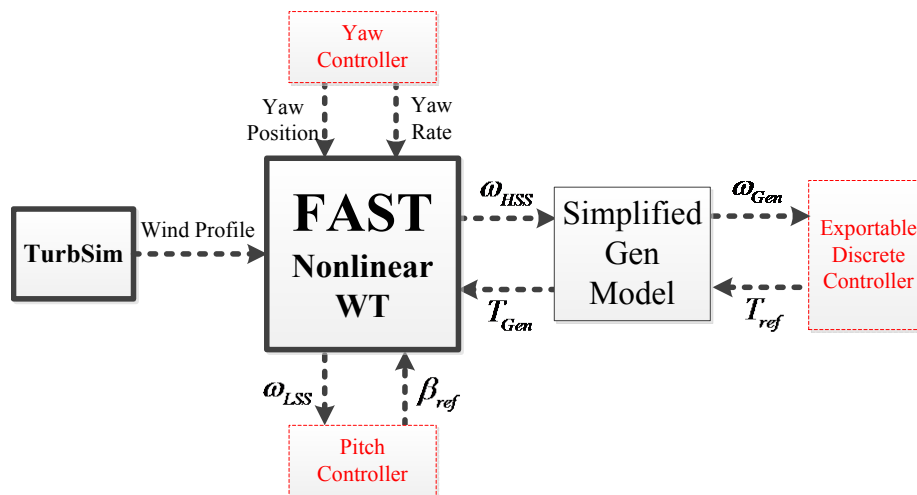
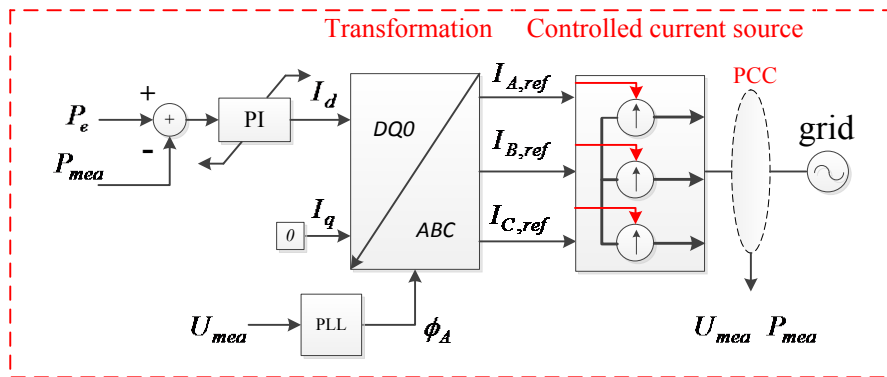


Figure 2. Layout of the CART3 model using FAST and TurbSim

We overwrote the parameters of the FAST input file with data for the CART3 parameters (e.g., the blade radius, hub height, and mass). The drivetrain was modeled in FAST with the measurable high-speed shaft and low-speed shaft rotating speed. The exportable discrete controller employs the MPPT control in the baseline mode, and new control concepts can be implemented in it. The FAST-based nonlinear wind turbine can be operated under the stochastic, full-field, turbulent wind speed profiles designed by TurbSim [13]. The wind turbulence intensity is a tunable setting in TurbSim; consequently, the researched wind turbine is evaluated with respect to various wind turbulences. After comprehensive case studies, the proposed control concept in the exportable discrete controller can be compiled and integrated into the CART3 SCADA system to control the real turbine, so new control concepts can be rapidly developed and tested based on the platform.

Power converters interface with the CART3 model and the connected power system grid. In our previous work [20], the simplified generator in the CART3 model was fully replaced with a detailed PMSG and back-to-back average power converter to constitute a complete CART3-PMSG integrated model. The PMSG and power converters can be either mathematically modeled or built-in blocks of SimPowerSystem in Simulink. To improve the real-time simulation efficiency of the RTDS, a simplified integration method is employed with the power electronics not modeled. Figure 3 presents the block diagram integrating the generated wind power into the electric grid. Because the voltage stability is maintained by the grid, the q-axis current is set to be zero to achieve the unity power factor mode. The d-axis current is regulated by a Proportional-integral (PI) controller according to the error between the electrical power reference and actual measured real power.



**Figure 3. Simplified interface between CART3 and the connected power system**

The FAST-based CART3 model was connected to the modeled power system using Simulink. The controlled-current sources in Figure 3 generated the real power according to the FAST high-speed shaft power measurement. The FAST program is a powerful simulation tool that can be used to evaluate the response of the wind turbine side—with respect to the electrical and mechanical components—to the events of the grid side, which consist of the components in the SimPowerSystem library.

### 3 Inertial Control Methods for Variable-Speed Wind Turbine Generators

As mentioned above, based on whether a frequency measurement exists or not, we divide the inertial control methods into two distinct categories, each of which presents different features for frequency support.

#### 3.1 Frequency-Based Inertial Control

The control logic for the FBIC response is presented in Figure 4. The filtered derivatives of the system frequency,  $df/dt$ , and frequency deviation,  $\Delta f$ , are multiplied by factors  $K_f$  and  $K_d$ , respectively. Then, this additional power is added to  $P_{MPPT}$  during the frequency excursion.

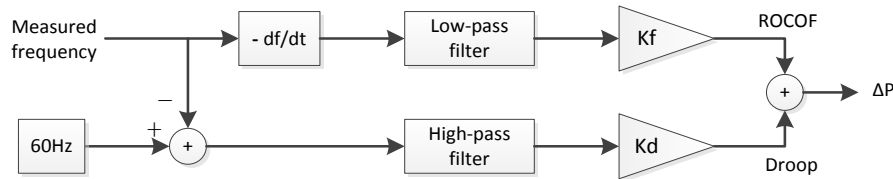


Figure 4. Simplified interface between CART3 and the connected power system

A low-pass filter with a 0.1-second time constant is added to process the ROCOF signal; therefore, the power or torque commands are smoothed to get rid of the severe transient loads caused by the noise. A high-pass filter with 10-second time constant is added to the droop-based term, so a constant frequency deviation cannot pass through, and the WTG recovers automatically when the settling frequency is attained. The ROCOF-based term is dominant at the beginning of the frequency dip, whereas the frequency deviation-based term is dominant when the frequency arrives at the nadir, so using the combination of the two provides a better response than using one [21]. The scale factors  $K_f$  and  $K_d$  are used to strengthen the inertial response of each term.

#### 3.2 Stepwise Inertial Control

The SIC method is capable of providing the maximum possible frequency support based on understanding the overproduction capability of variable-speed WTGs [22]. To protect the WTG system from damages, some restrictions must be respected during the inertial response. The minimum rotor speed ensures the stable operation of a WTG, so the inertial control mode will be stopped if the rotor speed hits the minimum limit. Because the electromagnetic torque is controlled by the stator current flowing through the power converter, the torque limit is set to 1.2 per unit (p.u.) to prevent damages to the insulated-gate bipolar transistors. Respecting the restrictions mentioned above, the inertial response can be shaped in terms of its magnitude and duration to satisfy different grid codes.

An improved SIC method is introduced by the authors of [11], which is called stable adaptive inertial control (SAIC). The power reference for SAIC is illustrated in Figure 5. The SAIC method is different from the conventional SIC method in that the temporary increased power reference does not remain constant but decreases in parallel with the MPPT curve. In fact, the power reference for the deceleration stage simply shifts upward from the original MPPT curve at a certain wind speed. This feature is essential to the improved frequency support performance

compared to the classic SIC method. Because the power reference decreases with the cubic function of the rotor speed, the decreasing rate is higher at the beginning and converges to zero at Point C, when the WTG operates in the quasi-stable state. Then a relatively small amount of deloaded power is required at Point C to accelerate the WTG. Later, the WTG is restored to its predisturbance MPPT operation at Point A as the rotor accelerates via D-E-A. A severe second frequency dip and overdeceleration can be effectively avoided because the WTG is stabilized at Point C, and a small amount of deloaded power ensures the WTG's acceleration. In addition, the stepwise increased active power is adaptive to the predisturbance rotor speed, so excessive kinetic energy extraction is avoided.

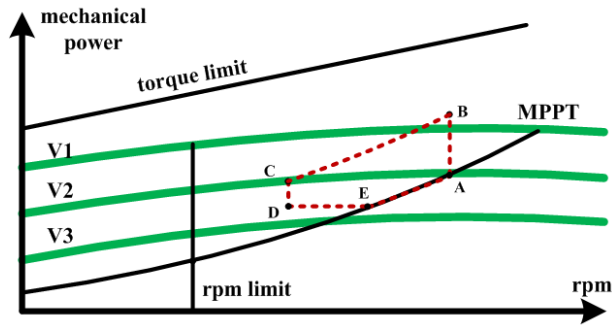


Figure 5. SAIC scheme in the rotor speed plane

Similarly, the second, improved SIC method adopted is known as torque-limit-based inertial control (TLIC) [10]. As illustrated in Figure 6, the power reference is defined in the deceleration (A-B-C) and acceleration (C-D-E-A) stages, respectively. When the frequency deviation is detected, the WTG output power will increase to Point B from the predisturbance Point A. The power reference at Point B corresponds to the torque limit and current rotor speed. The decelerating power reference will be regulated along B-C until the rotor speed is stabilized at the quasi-stable state at Point C. Later, power deloading is required to restore the discharged kinetic energy, and the WTG recovers to the predisturbance state in the acceleration stage. For the same reason, overdeceleration is avoided because the electromagnetic power reference decreases and intersects with the mechanical power reference. A relatively small amount of deloaded power is enough to accelerate the WTG while not causing a severe second frequency dip because the turbine is operated in the quasi-stable state at Point C.

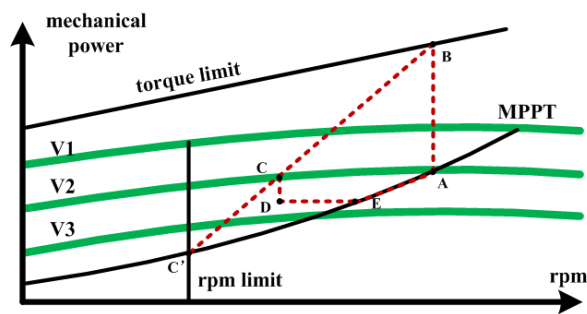


Figure 6. Scheme of TLIC in the rotor speed plane

A comparison of the typical SIC method to the SAIC method is further illustrated in Figure 7 in the rotor speed plane. The dashed black line represents the power reference for the typical SIC, in which the power boost is constant, and the wind turbine recovers to the MPPT operation directly when the frequency support is terminated. Because the power boost is kept constant in the typical SIC method, the difference between the electromagnetic and mechanical power increases as the rotor decelerates; therefore, the rotor tends to decelerate faster, and the wind turbine will be forced to stall when overdeceleration occurs. In addition, a larger power deficit occurs when the wind turbine begins to restore kinetic energy, which might cause a severe second frequency dip in the connected power system. By contrast, the two improved SIC methods avoid the issues of the typical SIC method with a flexible power reference.

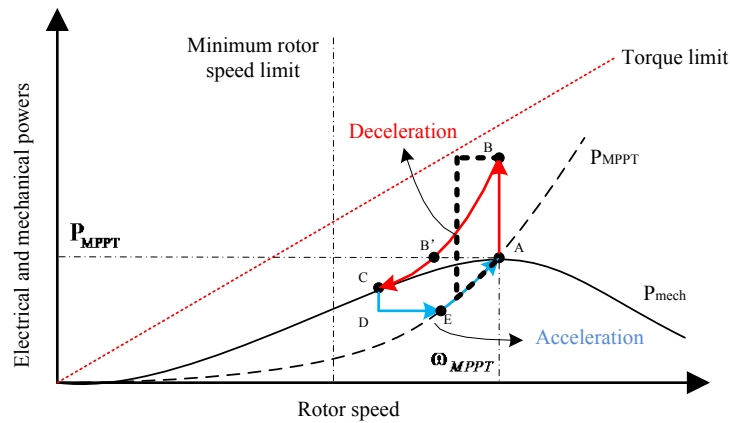


Figure 7. Comparison of the typical SIC method to the SAIC method

### 3.3 Comparison of Frequency-Based Inertial Control to Stable Adaptive Inertial Control

The SAIC method does not rely on the frequency measurement, and the magnitude and duration of the active power output can be shaped in the power-speed plane based on the specific system frequency regulation requirements and the WTG's capability. As a result, the SAIC method is more flexible and the response is faster and stronger compared to the FBIC method [10]. On the other hand, the FBIC method is characterized by the frequency measurement and simple implementation. The electromagnetic power reference for the SAIC and FBIC is compared in the rotor speed plane, as shown in Figure 8.

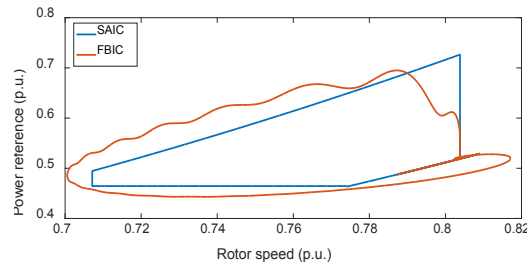


Figure 8. Comparison of SAIC to FBIC

Wind turbines employing the FBIC method recover to the MPPT mode without the explicit allocation of the deceleration and acceleration stages that are needed for the SAIC; thus, WTGs employing the FBIC restore the kinetic energy smoothly and automatically. Further, because the grid frequency is consistent in a power system, WPPs using the FBIC method regulate the grid frequency in coordination with other synchronous generators. By contrast, WPPs employing the SIC method regulate the output active power independently, hence a secondary frequency dip or frequency overshoot might be observed. The secondary frequency dip might be rather severe due to the inappropriate parameter design, especially when the WTG begins to restore kinetic energy by decreasing its power output when the initial frequency dip is not fully arrested [23].

### 3.4 Modification to the Torque-Limit-Based Inertial Control Method Considering Turbulent Wind Conditions

Difficulties arise when implementing these methods in a real wind turbine operating under highly turbulent wind conditions. In the TLIC method, the quasi-stable state at Point C needs to be detected before accelerating the WTG; however, the rotor accelerates and decelerates a lot due to the wind turbulence, so it is impractical to determine this point by monitoring if the rotor speed does not change much. In addition, maintaining a constant power reference ( $P_{DE}$ ) might fail to accelerate the wind turbine in case the wind speed decrease causes the available aerodynamic power to fall below the electromagnetic power. We modify the TLIC method to address these issues. The deceleration stage (A-B-C) is sustained for a predefined duration,  $T_{dec}$ . The power reference begins to decelerate the WTG as long as the deceleration is sustained for the precalculated duration. We designed the acceleration power reference according to the control logic shown in Figure 9, in which the power reference decreases by 0.08 p.u. per second until the rotor acceleration is detected.  $P^*$  is the power reference when the acceleration starts. During the acceleration stage, if the rotor acceleration is terminated by the decreased wind speed, the power reference will continue decreasing. The power reference will switch back to the MPPT mode when the acceleration power,  $P_{acc}$ , equals the MPPT power.

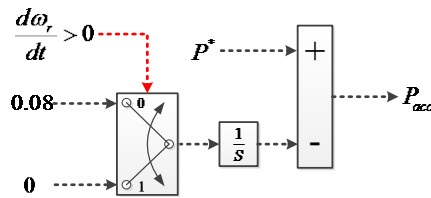


Figure 9. Control logic of accelerating the wind turbine in the modified TLIC method

## 4 Modified Western Electricity Coordinating Council Three-Machine, Nine-Bus Test Electric Grid

We employ a commonly used nine-bus power system [24] to test and compare the performance of various inertial control methods. Each generator is equipped with an excitation and governor to control the terminal voltage and system frequency in the model. We modify the original to facilitate the test. The frequency dip is triggered by removing one generator, thus creating a sudden reduction in generation level. Sections 5.1–5.3 focus on the schemes and parameters of the inertial controls and employ Scenario 1 as the test electric grid. Section 5.4, combined with the HIL test in Section 6, composes the two-stage inertial response evaluation, which considers realistic wind conditions and uses the test grid in Scenario 2.

### 4.1 Scenario 1: SG3 Is Modified at Bus 3

As shown in Figure 10, SG3 is divided into three small generators, and the WPP is connected to Bus 4, where Load 1 is located; the capacity of the entire power system is reduced to accommodate the capacity of the WPP to highlight the frequency regulation effects. A small generator, SG33, is tripped off to create the frequency event, after which the frequency can be stabilized and recovered by the implemented primary frequency control and AGC. (This is clearly shown in the grid frequency profile in Fig. 24.)

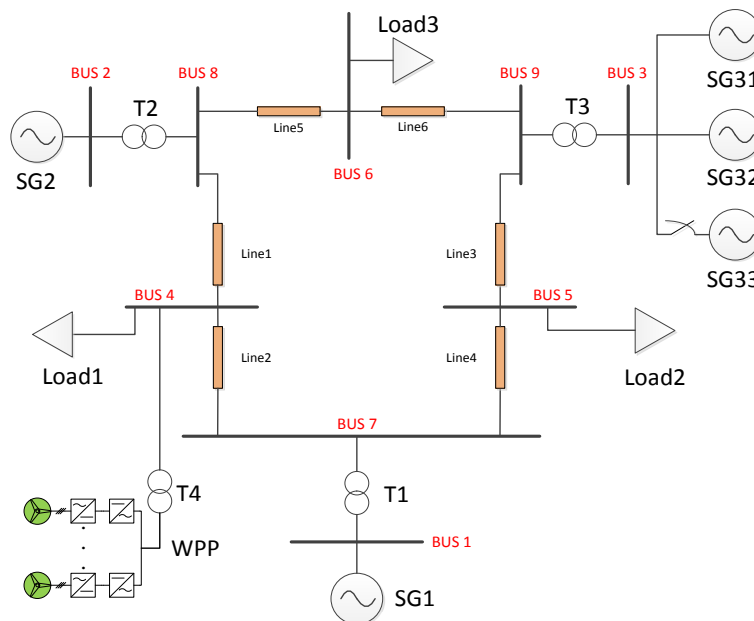
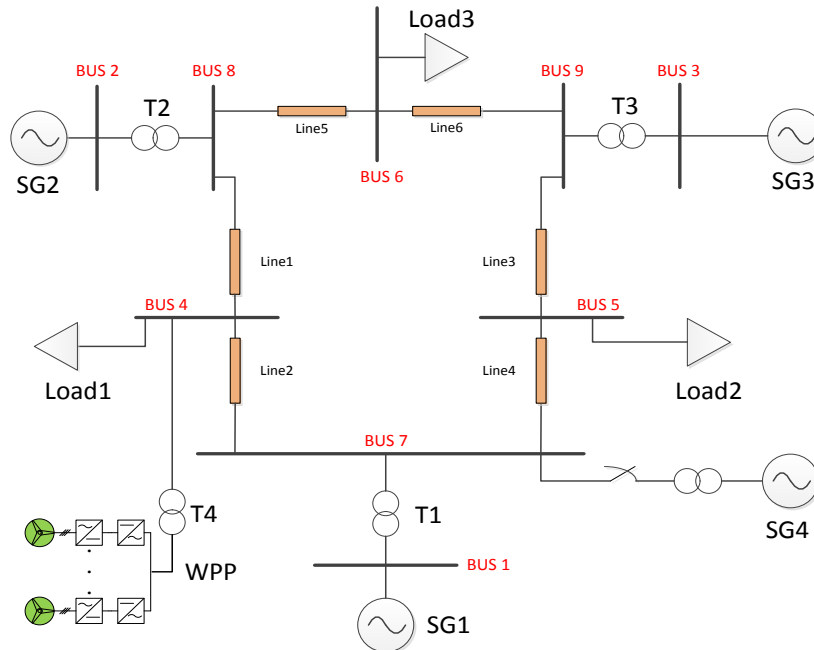


Figure 10. Modified nine-bus power system—Scenario 1

### 4.2 Scenario 2: SG4 Is Connected to Bus 7

Alternatively, the other modified configuration is adopted without scaling down the power system capability. The configuration of the test electric grid is presented in Figure 11, wherein a small generator, SG4, is connected to Bus 7 to trigger the frequency event.



**Figure 11. Modified nine-bus power system—Scenario 2**

By applying the wind power integration method mentioned in Section 2.4, the FAST-based CART3 model is connected to the test power system in Simulink. We apply active power control to the current sources to inject purely active power generated by the WPP. Assuming that the grid voltage is supported by synchronous generators, the current generated by the current source is synchronized to the grid voltage using a phase-locked loop. The high-speed shaft power of FAST is extracted to calculate the reference for the three-phase current sources.

## 5 Case Studies

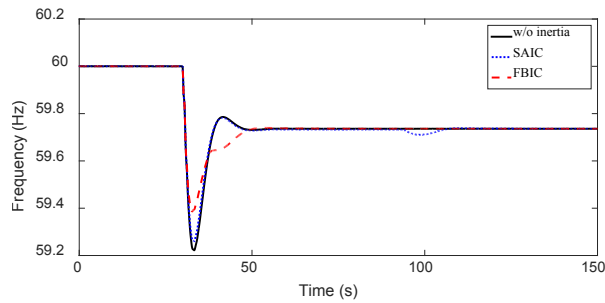
### 5.1 Comparison of Frequency-Based Inertial Control to Stable Adaptive Inertial Control in the Simulated Power System

Two different inertial control methods are implemented in the modeled test power system in Real Time Simulator Computer-Aided Design. Note that we employ the commonly used wind turbine model with the wind power coefficient modeled by the nonlinear function. The performance of the SAIC and TLIC methods are analyzed and compared in the case studies, with the application of Scenario 1 of the nine-bus electric power system. The parameters for the case studies are summarized in Table. 1. The rated wind speed is set to 11.2 m/s, and the two different wind speed conditions are 6.5 m/s and 11 m/s, respectively. The penetration level is defined as the proportion of the installed capacity of the WPP to the total installed capacity of the power system. In the low penetration level, less than 20%, the increased power generation of the WPP is consumed by the increased loads, so the capacity of Load 1 is tuned until the frequency is stabilized at 60 Hz before the event. SG2 is shut down in the high level of penetration, more than 20%, which is typical in many countries that have a high level of wind power penetration [4].

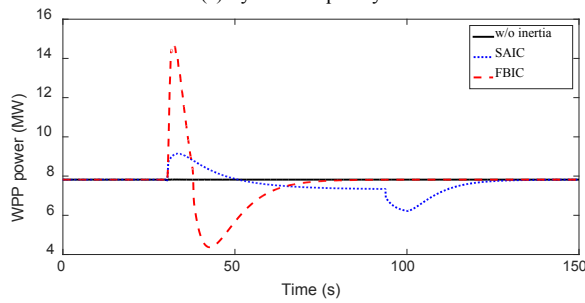
**Table 1. Scenarios for the Case Studies with Different Wind Power Penetration Levels and Wind Speeds**

Penetration	Wind speed	$P_{Load1}$ (MW)	$P_{sg1}$ (MW)	$P_{sg2}$ (MW)	$P_{sg31}$ (MW)	$P_{sg32}$ (MW)	$P_{sg33}$ (WM)
9.52%	Low wind	132	108	50	15	15	30
	High wind	132	100	32	12	15	30
30.9%	Low wind	160	157	-	15	15	30
	High wind	264	139	-	14	14	30

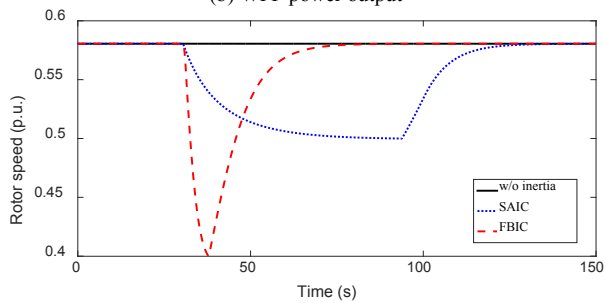
For SAIC, the stepwise power increase is set to be 30% of the predisturbance level,  $P_{mppt}$ , by trial and error. It ensures that the electrical power reference intersects with the mechanical power curve at the quasi-stable states in all wind speed conditions. For FBIC, the parameters  $K_f$  and  $K_d$  are both set to 30, which avoids excessive power extraction from the rotating mass. To prevent the wind turbine from stalling, the inertial response is disabled and the power reference is switched back to  $P_{mppt}$  if the rotor speed hits the minimum rotor speed of 0.4 p.u. In each case, the system frequency (Hz), power output of the WPP (MW), and rotor speed (p.u.) are plotted for comparison. The solid black line represents the baseline without the inertial response. The dashed red line and dotted blue line represent SAIC and FBIC, respectively. The torque limit is set to be 1.2 p.u., and the power rate limit is set to be 0.45 p.u./s in the simulation. The simulation results are presented in figures 12–15.



(a) System frequency

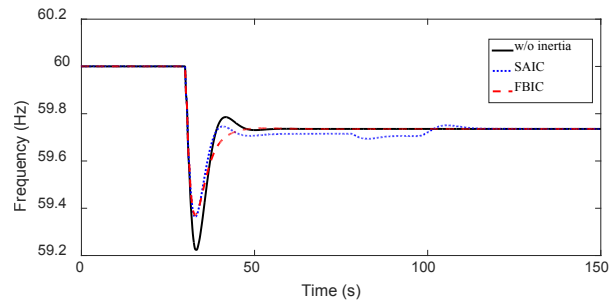


(b) WPP power output

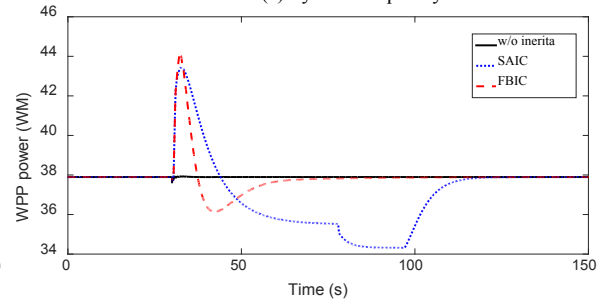


(c) Rotor speed

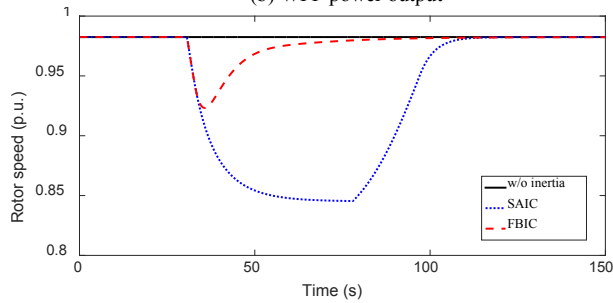
**Figure 12. Results for 9.52% penetration under low wind speed**



(a) System frequency



(b) WPP power output



(c) Rotor speed

**Figure 13. Results for 9.52% penetration under high wind speed**

In the cases of the low wind power penetration level (9.52%), FBIC improves the frequency nadir much more than SAIC, especially in the low wind speed condition. Because the wind speed increases in the high wind condition, SAIC and FBIC improve the frequency nadir to the same extent. The stepwise power increase of SAIC depends on the predisturbance  $P_{mppt}$ , so the extracted additional power is limited in the low wind speed; whereas the power increase of SAIC equals that of FBIC in the high wind speed. For the FBIC method, the increased power is almost the same with different wind speeds because the power boost is decided by the frequency excursion. Consequently, the frequency nadirs are almost the same in different wind conditions. Note that in the low wind speed case, the rotor speed hits the minimum rotor speed limit with FBIC due to the excessive kinetic energy extraction. A sudden power decrease follows as the power reference switches back to the  $P_{mppt}$  that is decided by the current rotor speed; however, the sudden output power deficiency does not lead to a severe second frequency dip, as shown in Figure 12(a), because of the low penetration level in this case. On the other hand, the rotor deceleration lasts longer with the SAIC method. Because the rotor speed keeps decreasing, the electrical power output becomes smaller than it is in the predisturbance  $P_{mppt}$ , which is

undesirable because a long period of power underproduction occurs; therefore, the turbine needs more time to recover after the deceleration and acceleration, during which the frequency is lower than the settling frequency, as shown in Figure 13(a).

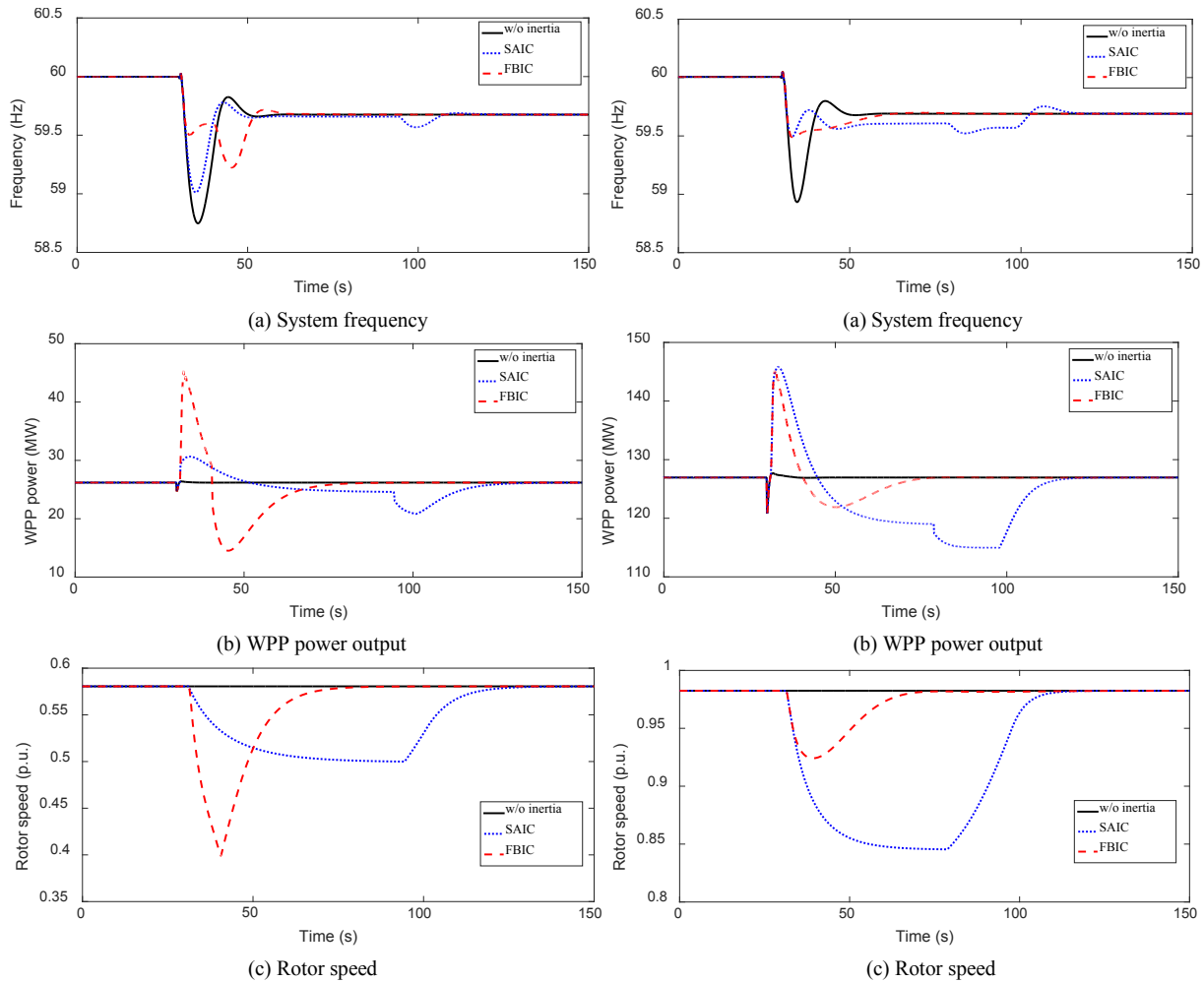


**Figure 14. Results for 30.9% penetration under low wind speed**

**Figure 15. Results for 30.9% penetration under high wind speed**

In the cases of the high wind power penetration level (30.9%), SG2 is shut down due to the tremendous wind power increases. It seems that the total system inertia decreases, and severe frequency excursions are more likely to happen than in the case of the low penetration level. Under the low wind speed condition presented in Figure 14(a), a severe second frequency dip occurs with the FBIC method, and the dip can be even larger than the initial frequency drop caused by the event. In contrast, the SAIC method does not lead to a similar problem because the stepwise power increase is set adaptively to different wind conditions. In fact, SAIC produces a small second frequency dip in all of the case studies. Further, in the high penetration case the FBIC and SAIC methods improve the frequency nadir much more than the baseline without inertial response. Figure 14(a) and Figure 15(a) show that the frequency nadir is improved more

than 59.5 Hz by FBIC. Note that in some areas in the United States 59.5 Hz is a significant value to trigger underfrequency load-shedding relays [23], which indicates the need for WPPs to provide frequency regulation—particularly in scenarios of high wind power penetration levels. Last but not least, because the injected electrical power is regulated naturally according to the change of frequency in a manner that is similar to that of conventional synchronous generators, the frequency settles smoothly with FBIC; essentially, the FBIC method can provide some damping effect, as demonstrated in [25].

## 5.2 Impact of Scaling Factors on the Performance of Frequency-Based Inertial Control Method

In this section, we discuss the impact of the scaling factors  $K_f$  and  $K_d$  on the performance of the FBIC method.  $K_f$  and  $K_d$  range from 0–60 in the case studies. We use the frequency nadir, ROCOF, and recovery time as metrics to evaluate the performance of the FBIC method. Note that the duration from the beginning of the event to the time that the system frequency settles down is defined as the recovery time. The hollow points in each figure are original data points from the experiments, and other data points are obtained using interpolation methods.

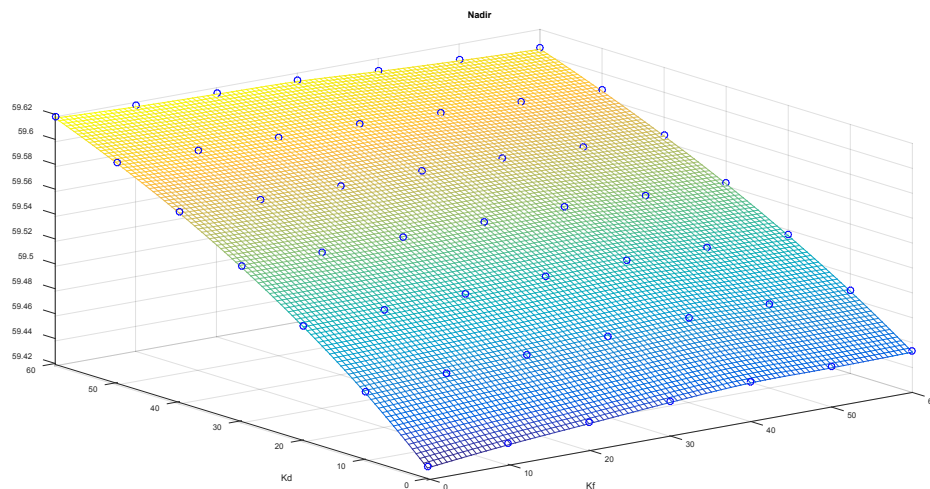


**Figure 16. Frequency nadir with respect to different scaling factors**

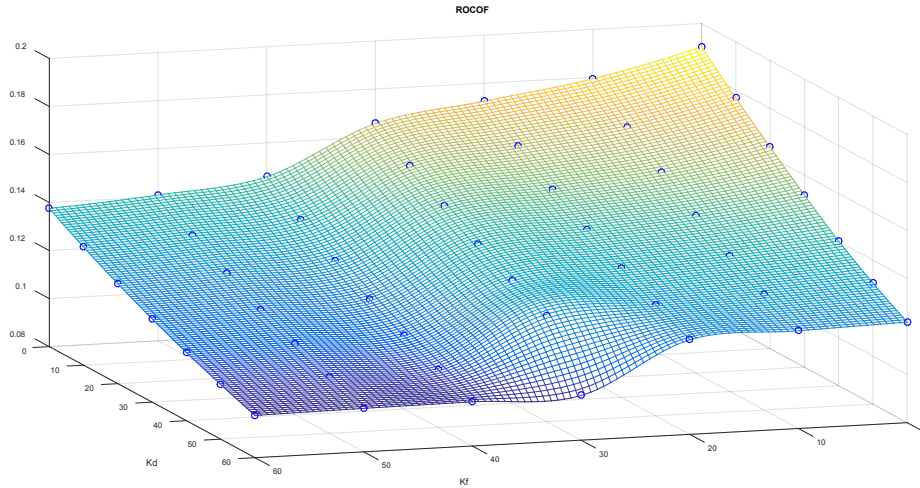


**Figure 17. ROCOF with respect to different scaling factors**

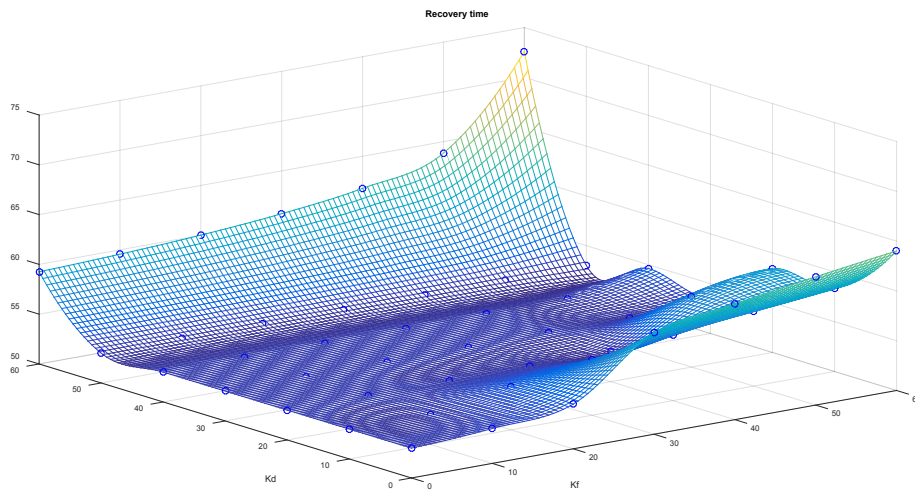


**Figure 18. Recovery time with respect to different scaling factors**

Figure 16 shows that the frequency nadir is influenced by different  $K_f$  and  $K_d$  values. It is evident that the frequency nadir improves a lot with an increasing value of  $K_d$  because more power is released. In contrast, the frequency nadir is not improved significantly with the increasing  $K_f$  because  $df/dt$  reacts at the beginning of the frequency droop and decreases to zero when the frequency is arrested at the frequency nadir. Therefore, the derivative has a fast response, whereas the deviation has a slow response, and using each part is inferior to the performance when using the combination of both. In the ROCOF presented in Figure 17,  $df/dt$  and  $\Delta f$  both contribute to supporting the frequency as the ROCOF decreases with the increased values of  $K_f$  and  $K_d$ .

The recovery time presented in Figure 18 shows that the duration tends to be extended when  $K_f$  is increased. That is because more energy is released with a larger  $K_f$ , so more time is needed to restore the rotor speed. Note that when  $K_f$  ranges from 30–60, the recovery time decreases with increasing  $K_d$  values because of the damping effect due to a larger  $K_d$ ; however, when  $K_d$

increases further, the recovery time becomes longer. This might be because a large value of  $K_d$  tends to cause additional frequency oscillations in the power system [25].

### 5.3 Impact of Slope Values on the Performance of the Torque-Limit-Based Inertial Control Method

As shown in Figure 19, the slope values for the deceleration stages impact the inertial response of the TLIC method. Line BC1 corresponds to the gradual slope, and Line BC3 corresponds to the steep slope. The values of the slope are selected from the range between BC1 and BC3. The most gradual slope is determined such that C1 corresponds to the minimum allowable rotor speed.

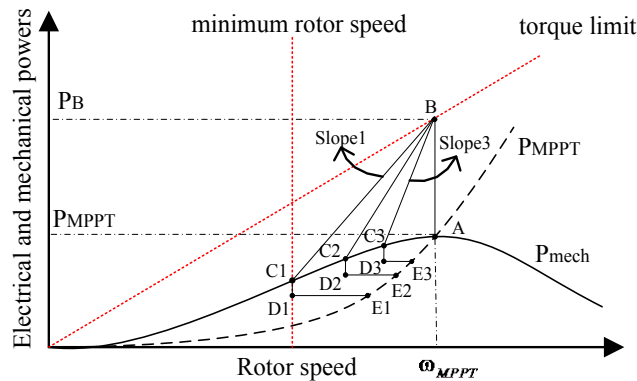


**Figure 19. Illustration of different slope values in the TLIC method**

This phenomenon is tested under different wind speed conditions: 8.2 m/s, 9 m/s, and 10 m/s. The frequency dynamics and power-speed characters under different wind speed conditions are presented in figures 20–22. Note that the red dotted-dashed line corresponds to the gradual slope, and the black dashed line corresponds to the steep slope. The blue dotted line refers to the slope value in the middle.

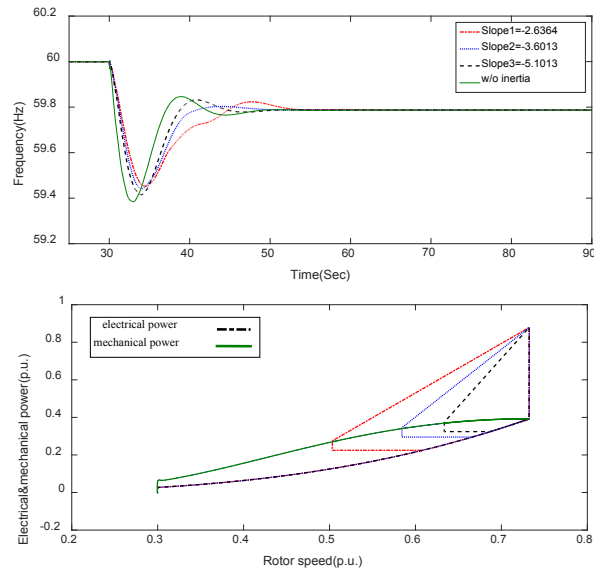


**Figure 20. Frequency profile and power-speed characteristics when the wind speed is 8.2 m/s**

The frequency nadir, ROCOF, and recovery time are selected as metrics for different scenarios. The inertial response improves the frequency nadir and restricts the ROCOF in the meantime. The improvement of the frequency nadir reduces the probability of a disconnection from the grid due to the tripped underfrequency relay protection. The final frequency does not fully recover to the prefault value because of the linear nature of the droop control of the remaining synchronous generators and because AGC is not implemented in the model system.

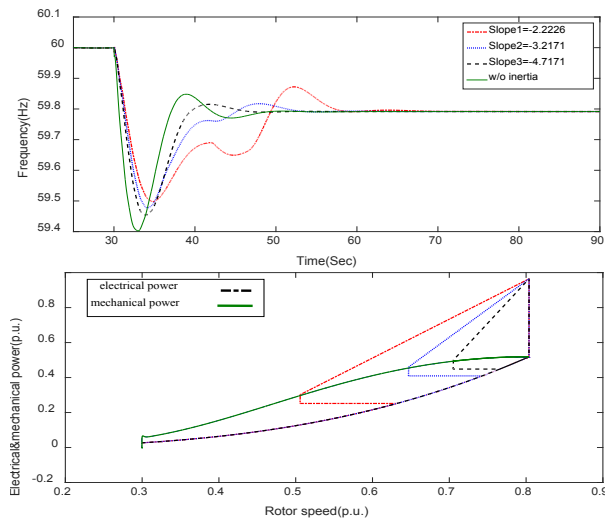


**Figure 21. Frequency profile and power-speed characteristics when the wind speed is 9 m/s**

In addition, the recovery time tends to be longer when the slope changes from steep to gradual. The extension of the recovery time is undesirable because it delays the recovery of the grid frequency to the scheduled value. TLIC exploits the maximum frequency support capability of the WTG, and the released energy is considerable throughout this duration, especially when the rotor speed reaches the minimum possible value along the gradual slope; however, the recovery time is extended a lot with this gradual slope, which is obvious in high wind conditions, as

shown in Figure 21 and Figure 22. As a result, there is a trade-off between the frequency nadir (ROCOF) and recovery time. The selection of slopes should be thoroughly considered with respect to the power system configuration and acceptable ranges of recovery time.

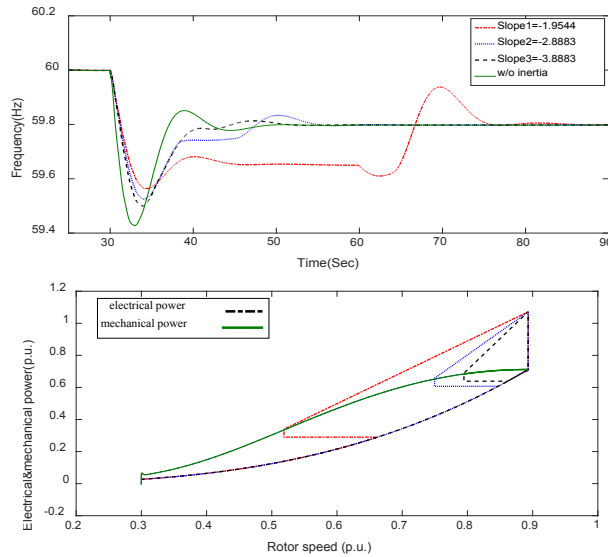


**Figure 22. Frequency profile and power-speed characteristics when wind speed is 10 m/s**

## 5.4 Assessment of Inertial Response Under Highly Turbulent Wind Conditions

In most of the literature [20]–[22], [26], the wind speed is assumed to be constant during the inertial response. The reason for this assumption is because the inertial response is expected to be sustained for a few seconds, during which the wind speed might not change much; however, the inertial response of variable-speed WTGs can be sustained for more than 10 seconds with flexible control methods. In addition, the operating range of the rotor speed is wider for a wind turbine. In this context, it is not reasonable to test the inertial response under constant wind speed conditions. Taking advantages of the powerful simulation tools developed by NREL, the inertial control methods are assessed and compared under highly turbulent wind conditions. We connect the FAST-based CART3 model to the test power system simulated in Simulink. The wind speed profiles with different turbulence intensities are generated using TurbSim. The electric power and rotor speed data of CART3 are collected; and the mechanical variables, such as the bending moments on the tower and blades, are evaluated. With the developed simulation model, the inertial control methods are researched comprehensively, which ensures the effectiveness and safety of the field test in the next step.

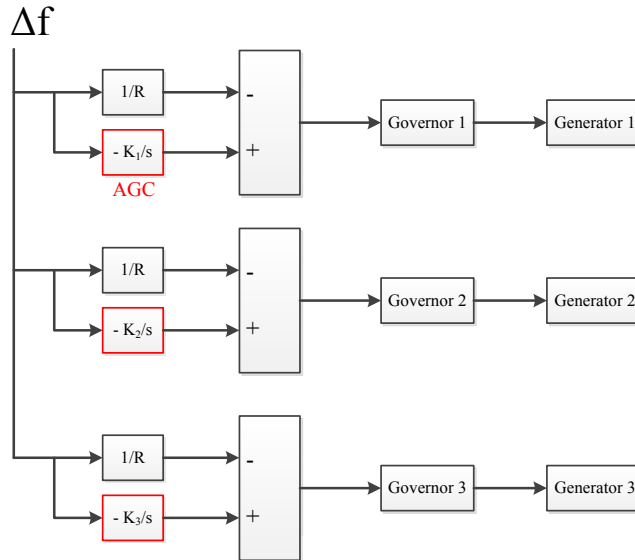


**Figure 23. Diagram of AGC**

To emulate the actual frequency response of a power system, the inertial response, primary frequency response, and AGC are implemented in the modeled test system. The AGC is implemented according to the configuration shown in Figure 23. Although AGC is deployed in a complicated means in a real power system, it is essentially determined by using proportional-integral controllers in a stand-alone power system. AGC is slower than droop-based primary frequency response, which can be realized by tuning the AGC gain,  $K_i$ , in the diagram. The droop coefficient  $R$  is set to 20% for each synchronous generator. The AGC gains are identical for each synchronous generator, which is tuned to be 1 by trial and error because AGC typically takes effect 30 seconds after the frequency event.

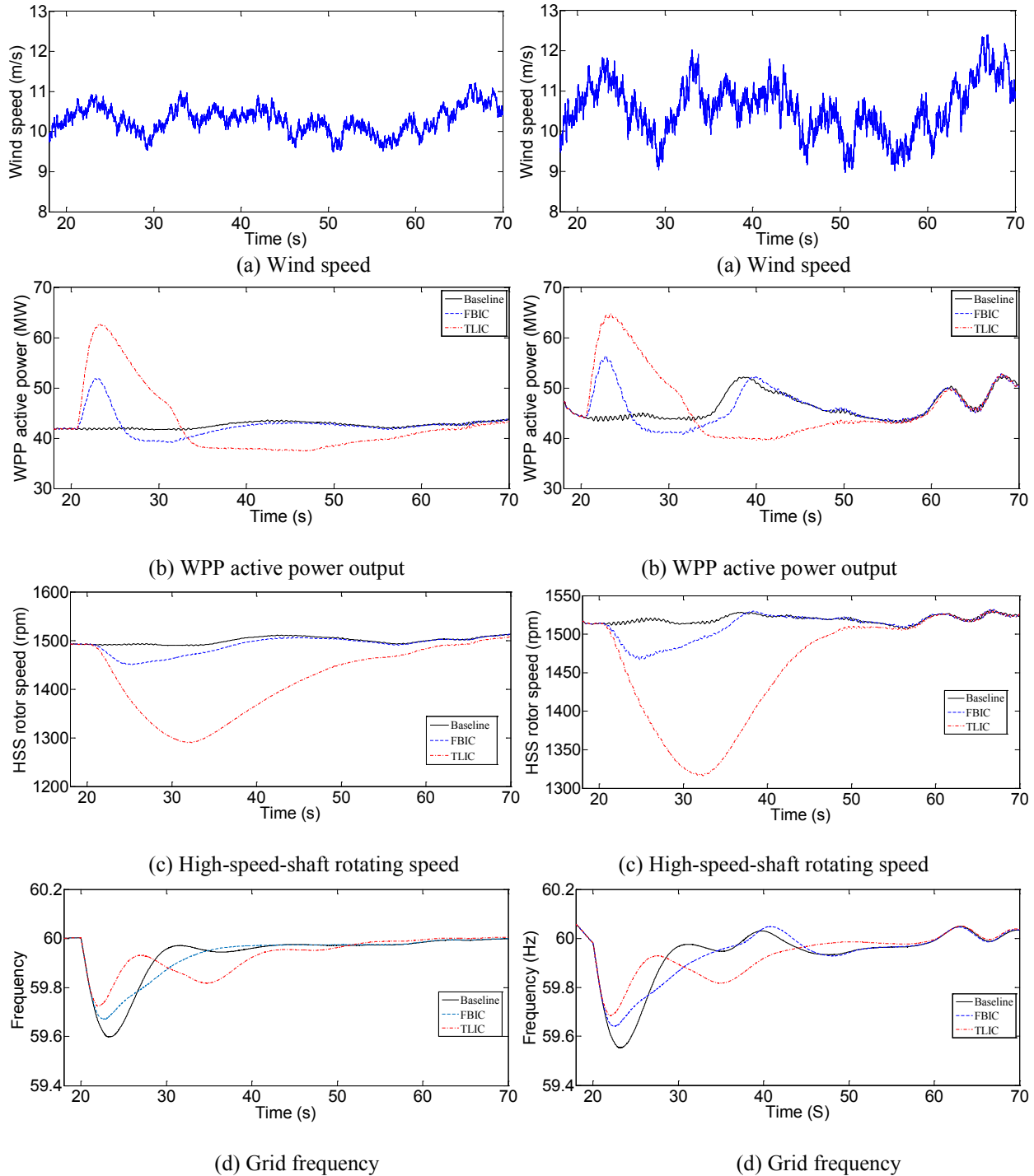


**Figure 24. Inertial response of CART3 under turbulent wind intensity 5%**

**Figure 25. Inertial response of CART3 under turbulent wind intensity 10%**

The FBIC and TLIC methods are compared to the baseline control. The turbulence intensities are set to 5% and 10% in the two cases, so it is obvious that the wind speed profile shown in Figure 25(a) is more turbulent than that shown in Figure 24(a). For the FBIC method, we employ the measures in [26] to determine the scale factors for the derivative and deviation terms. Considering the ROCOF term first, the maximum kinetic energy released through this loop is associated with the most severe frequency deviation in the electric grid, as denoted in (5):

$$\Delta E_{ROCOF} = K_f \int \omega \frac{d\omega}{dt} = \frac{K_f}{2} (1 - \omega_{s,min}^2) \quad (5)$$

where  $\omega_{s,min}$  is the predefined minimum per-unit synchronous speed within the power system. The maximum releasable kinetic energy of a wind turbine is associated with the predisturbance rotor speed,  $\omega_{r0}$ , as denoted in (6):

$$\Delta E_k = H (\omega_{r0}^2 - \omega_{min}^2) \quad (6)$$

where  $\omega_{min}$  is the minimum wind turbine rotor speed, all per unit. The discharged energy comes from the kinetic energy stored in the rotating mass, so  $K_f$  equals:

$$K_f = \frac{2H (\omega_{r0}^2 - \omega_{min}^2)}{1 - \omega_{s,min}^2} \quad (7)$$

For the frequency deviation-based loop,  $K_d$  is simply set to 20, which is consistent with the droop parameter of other synchronous generators, so the WPP shares the loads with other synchronous generators according to their capacities. The value of  $\omega_{s,min}$  is set to 0.95 in the simulation.

According to Figure 24(c) and Figure 25(c), in the highly turbulent wind conditions the rotor speed recovers successfully after the kinetic energy is released. The modified TLIC method solves the previously mentioned issues. Comparing the active power boost provided by the WPP, CART3 discharges more power to support the grid frequency with the TLIC method, as shown in Figure 24(b) and Figure 25(b). The active power boost from CART3 is faster and stronger with the TLIC method, and as a result the frequency nadir is improved much more compared to that of the FBIC method; however, the TLIC method extracts the kinetic energy by regulating the wind turbine close to its overproduction limit, so the rotor speed decelerates more in both cases, and it takes longer to restore the kinetic energy in the rotating mass. In addition, a larger power decrease tends to accelerate the rotor speed faster; however, a second frequency dip might be observed. As presented in Figure 24(d) and Figure 25(d), a small second frequency dip happens in the scenarios with the TLIC method; in contrast, the grid frequency recovers to the nominal value smoothly in the scenarios with the FBIC method.

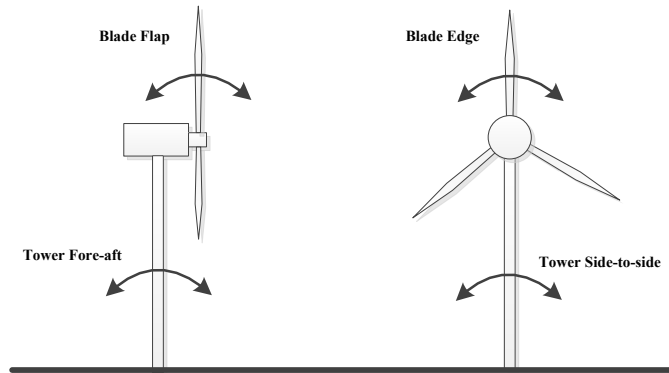


**Figure 26. Illustration of the loads on the wind turbine mechanical components**

The impact of the inertial control methods on the wind turbine's mechanical components are examined in the simulation. An appropriate inertial control method should not cause excessive structural loads, which tend to shorten the lifetime of a real turbine. We analyze the load variables collected from FAST, and the interested loads are illustrated in Figure 26. According to Figure 27, the inertial response increases the side-to-side bending moment of the tower, and the blade flapwise bending moment almost stays the same with the inertial response. In contrast, the inertial response can reduce the loads on the edgewise of the blade; in addition, the tower fore-aft bending moment is also reduced. This might be because the wind turbine is operated with a suboptimal power coefficient when the inertial response is released. In this situation, the loads on the wind turbine components are mitigated by allowing more wind to pass through the turbine blades, so the thrust force of the wind is reduced. In fact, the excessive loads caused by the inertial response can be omitted compared to the lifetime fatigue loads on the wind turbine. Comparing the FBIC method to the TLIC method, the higher loads caused by the TLIC method are much more evident. More detailed testing should be performed to assess the impact of the inertial response on the wind turbine's lifetime fatigue loads, such as the results presented in [19].

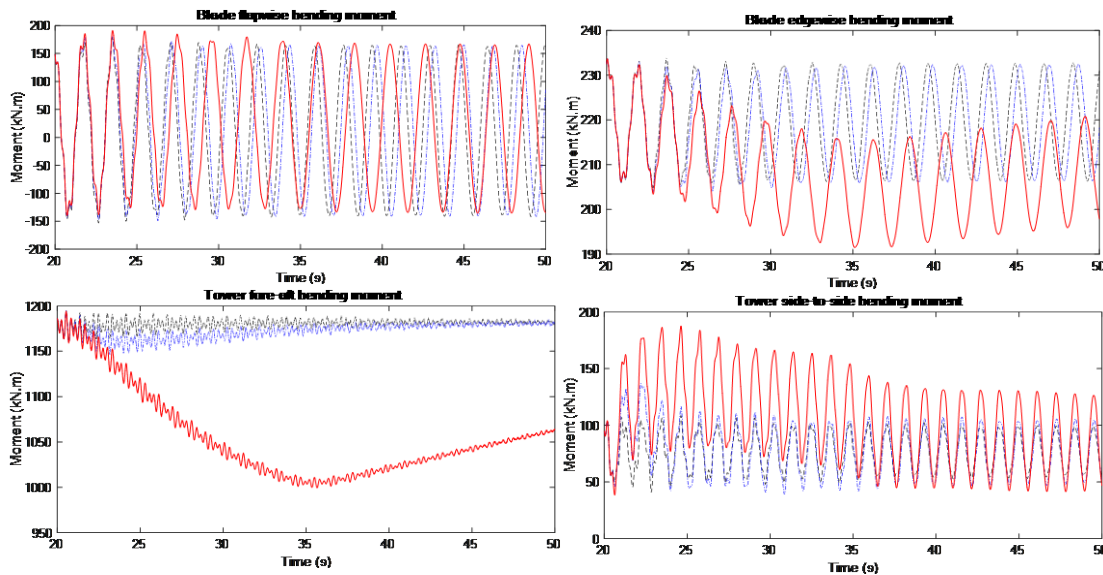


**Figure 27. Impact of inertial control methods on the wind turbine components**

## 6 Field-Testing Using Hardware-in-the-loop Techniques

After completing the comprehensive case studies in the off-line simulation, we propose a real-time simulation with HIL techniques. Commonly, off-line simulations are essential to test the performance of a wind or photovoltaic system with the embedded control concepts. With increasing penetrations of renewable energy and the development of advanced power electronics-based interconnection systems, electric power systems are becoming more complex; thus, pure software simulations are not adequate to transfer technology from the experimental phases to prototypes and products [27]. Renewable energy systems are exposed to various situations related to their interconnection to electric power systems, and comprehensive and strict standards guide the safe integration of renewable energy [28]. In this context, a hardware-based simulation and test should be considered in which the hardware under test (HUT) is validated against various noises and transients that might be encountered in the field. The performance and response of the test article should comply with the grid codes before large-scale integration is implemented. Constructing the complete hardware test bed, including all the physical parts, is a time-consuming and expensive task in the laboratory environment; in addition, the flexibility and scalability of the pure hardware test system are limited. To develop a cost-effective and reliable platform to validate the renewable energy integration issues and the proposed control concepts, HIL techniques are gaining increased attention. The HUT is evaluated under a simulated test model, which is implemented using a digital real-time simulator (DRTS). As the simulated model is executed in real time, the analog signals from the HUT are received and calculated by the model, and then the simulated model updates the states and sends the digital signals to the HUT within the same step. This sequence of interactions between the HUT and the real-time simulated model is completed at each time step, which emulates the HUT operating in a pure hardware system. Note that a smaller time step will benefit closed-loop simulation by capturing the dynamics and reducing the time delay introduced by the power amplifier and digital/analog (analog/digital) conversion; however, the time step cannot be reduced arbitrarily because it is restricted by the scale of the simulated power system and the computation ability of the processors.

Digital real-time simulations are commonly categorized into four types according to [29]: real-time software-only simulation, using a DRTS as a hardware controller, controller hardware-in-the-loop (CHIL), and PHIL schemes. First, using the real-time simulator only as a simulation tool is usually the initial step to complete an HIL test. As discussed in the example presented in Section 5.1, inertial control methods are evaluated and compared in the nine-bus power system using the DRTS. The simulation results demonstrate the effectiveness of the proposed control methods in the test power system. Later, signals from the modeled wind turbine are replaced with those received from a real one at each time step.

Second, the real-time simulator can be used as the controller for the hardware. In the wind power industry, using the DRTS to control the dynamometer is an example of this type of HIL application [30]. The test article rotates with the dynamometer via the same drivetrain. In fact, the dynamometer is a motor that can be controlled by the DRTS in terms of its rotating speed and mechanical torque references. In doing so, the aerodynamic torque generated by the wind turbine blades can be designed and controlled in the laboratory environment such that it is not necessary to install the test article (wind turbine generator) onto the tower. In addition, by using the DRTS-

controlled dynamometer, any transients on the shaft caused by the wind can be designed and implemented easily; waiting for a specific wind condition in a real system might consume much more time.

Further, with extensive research on wind and photovoltaic systems, CHIL and PHIL simulations are gaining popularity. In the CHIL simulation method a real-time software model is connected in a closed-loop with a physical controller (the HUT in this configuration). CHIL simulations are commonly used to test controllers for power electronics-based systems and to validate protection relay settings and performance [28]. The controller can be validated under a variety of operating conditions that are easily designed in the real-time simulator, helping to reduce the of risk controller deployments in actual power systems.

In PHIL simulations, which are commonly employed to test the integration of renewable energy, the HUT is interfaced with the simulated electric power systems at a higher voltage or power level. Because the HUT is a power device that sinks and sources power, a power amplifier is required. It provides the real electric dynamics to the HUT according to the dynamics at the PCC in the simulated model. By leveraging the powerful test capability of PHIL simulation, the response of renewable energy systems can be tested under different electric power system contingencies, which are rather rare but can be destructive in a real power system. The accuracy and stability of the closed-loop PHIL simulation must be carefully considered. The authors of [31] demonstrate how to implement appropriate interface algorithms and compensation techniques for one particular PHIL experimental configuration.



**Figure 28. NREL's CART3 (left) and CART2 (right). Photo by L.J. Fingersh, NREL 19937**

In this section, the CHIL techniques are employed to test the inertial response of a real wind turbine, CART3 (shown in Figure 28), located at the NWTC at NREL, in Boulder, Colorado. As discussed in Section 2.4, NREL engineers developed a detailed CART3 model based on FAST (Figure 29). The proposed control algorithms are compiled to a dynamic link library file in Simulink, which can be embedded into CART3's SCADA system to control the real wind turbine. In doing so, the wind turbine control strategies can be designed and tuned to take advantages of the code transformation between MATLAB and LabVIEW.

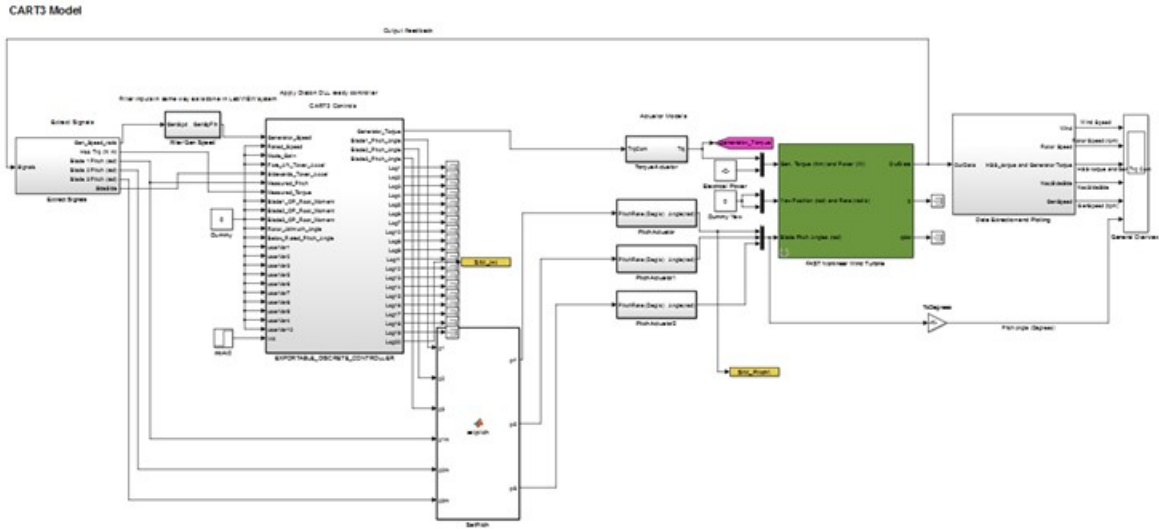


Figure 29. FAST-based CART3 model in Simulink

The test power system is modeled in the RTDS, and the frequency signal at the PCC is sent to the CART3 SCADA system (as shown in Figure 30). If the frequency deviation exceeds the deadband and it is detected by the inertial control system, CART3 will release kinetic energy and increase its active power output. The measured electric line power of CART3 will be sent back to the RTDS to complete the closed-loop simulation. Three-phase, controlled-current sources in the real-time software model then inject the same amount of active power into the simulated system. Here we assume unit power operation of the WPP, and the references for the controller current sources are calculated based on the active power measurement from CART3 and the measured voltage at the PCC in the model.

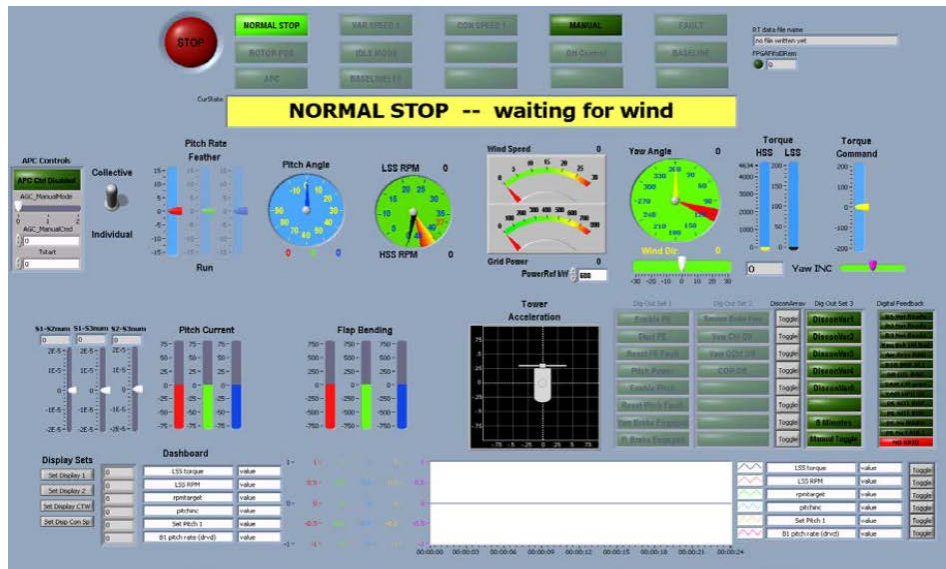
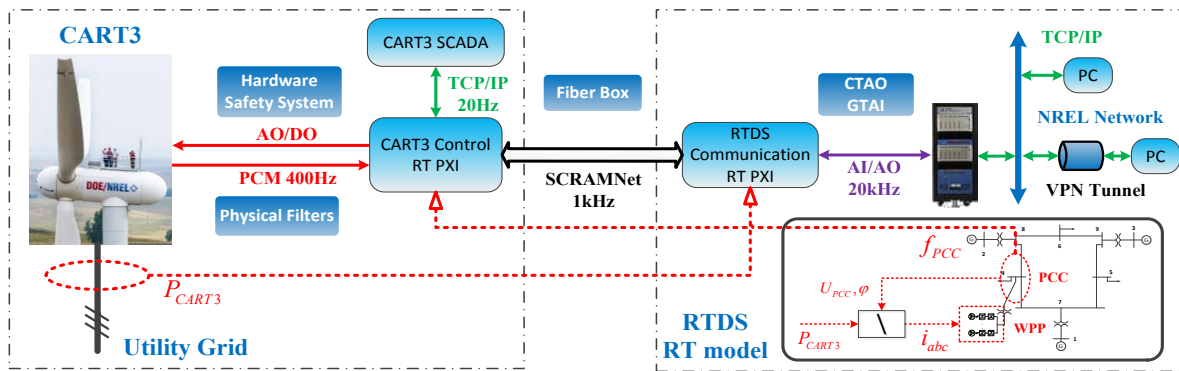


Figure 30. User interface of the CART3 SCADA system

The configuration of the CHIL test system is shown in Figure 31. Note that there is no power loop in the simulation, and all the exchanged signals are at low-voltage and low power levels,

although the actual CART3 is included in the simulation loop. The grid frequency is measured at the PCC in the real-time emulated power system in RTDS, and this frequency signal is sent to the CART3 SCADA system, which includes the implemented frequency-controlled inertial response. In the case of a grid frequency excursion outside of the deadband (0.2 Hz), CART3 will output its inertial response according to the implemented algorithms. The active power output of CART3 is measured by the power meter, and this signal is fed back to a current source in the real-time model to complete the closed-loop simulation. The CART3-side National Instruments real-time PXI controls CART3 and communicates with the SCADA. We set up additional communication cards in the CART3-side PXI and RTDS-side PXI to handle the communication between the two remote PXIs based on the SCRAMNet protocol.



**Figure 31. Configuration of the CHIL test system**

The test scenario begins with opening the generator SG3 output breaker in the simulated power system shown in Figure 11, which causes a system under frequency disturbance. This frequency event is then measured by the controller on the CART3 SCADA, which then commands the wind turbine's inertial response accordingly. Figure 32 shows the inertial response of CART3 when the FBIC method is activated. According to the figures, CART3 increased its active power output when the frequency excursion is detected. The wind turbine restores the kinetic energy and recovers to the MPPT after the inertial response.

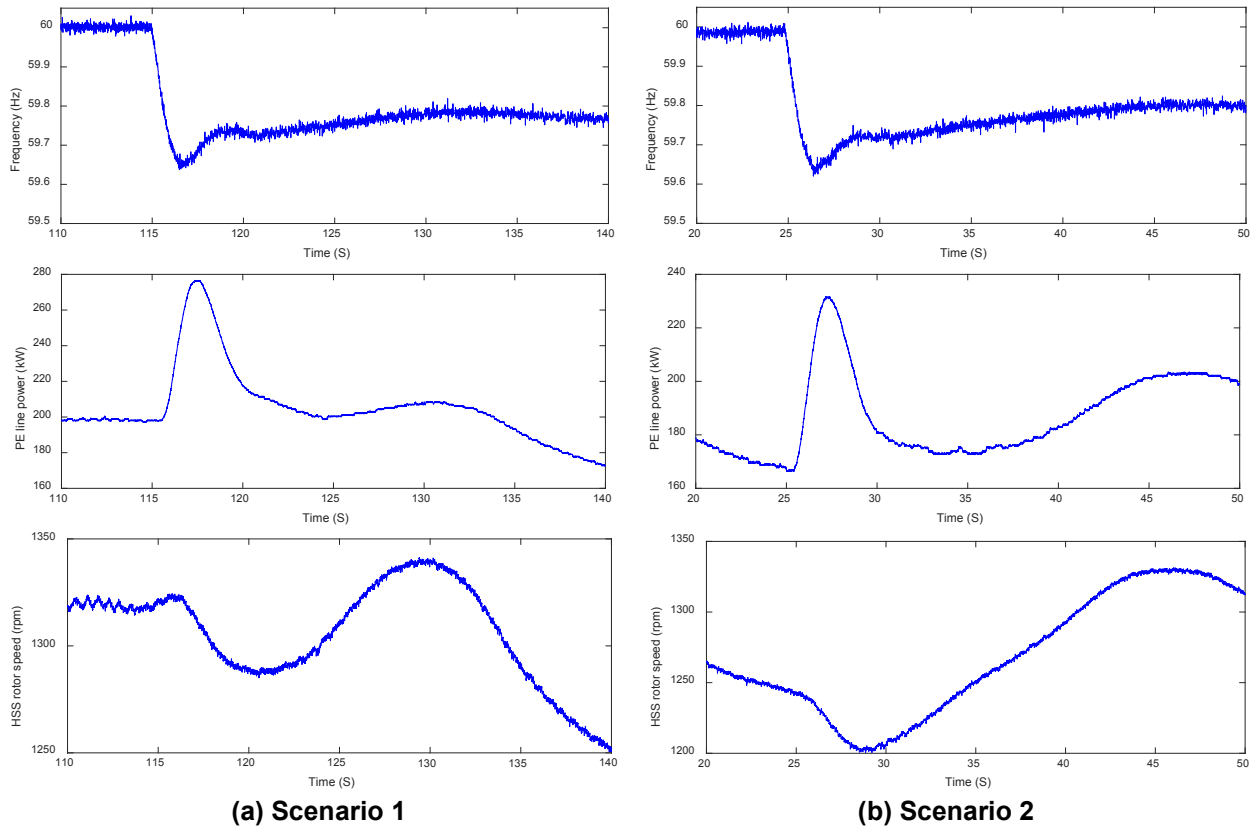


**Figure 32. CART3 inertial response with FBIC method—Scenario 1 and Scenario 2**

Later, the TLIC method is selected. The CHIL simulation results for this scenario are presented in Figure 33. In contrast to the FBIC method, more active power is released in this method to support the grid frequency. As a result, the rotor speed decelerates more, and it takes longer to restore the kinetic energy in the rotating mass. It is obvious that the inertial response of the wind turbine is stronger compared to that of the FBIC method. The active power can be doubled with respect to the predisturbance level. Note that when the rotor speed is approximately 0.4 p.u., the SCADA system will kick in and command an increase or decrease the electromagnetic torque on the turbine shaft. This helps CART3 pass the specific rotating speed quickly. The specific rotating speed is consistent with the natural frequency of CART3, which is harmful to the mechanical components because the resonance tends to increase the vibration.

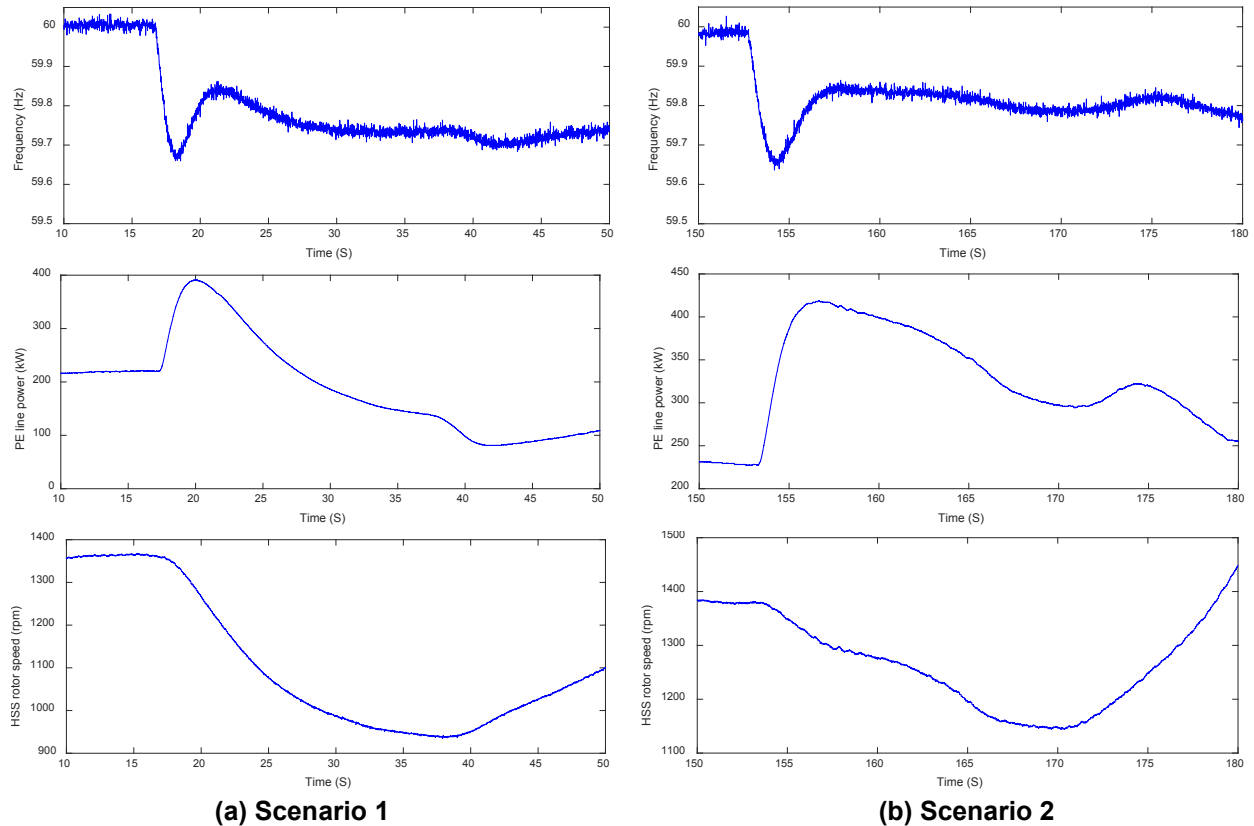


**Figure 33. CART3 inertial response with TLIC method—Scenario 1 and Scenario 2**

Note that the power loop is actually open in the presented CHIL simulations because CART3’s output is connected to a static utility grid instead of a power amplifier controlled by voltage from the real-time power system model. However, a CGI was commissioned at the NWTC at NREL in 2016 that can function as a 7-MVA power amplifier and be connected to CART3. Additional efforts are required to connect CART3 to the CGI at such a high power level (600 kW); for example, certain types of WTGs under test can provide current up to ten times higher than its normal rating under abnormal conditions for a short time period. In the future, the CHIL simulation will be extended to a complete PHIL simulation at full power level, in which the CGI functions as a power amplifier that sinks or sources the power generated or consumed by CART3 or other megawatt wind turbines located at the NWTC. The inertial response is tested using an industry-level wind turbine with respect to the frequency excursion occurring at the PCC. The configuration of the PHIL simulation is shown in Figure 34.

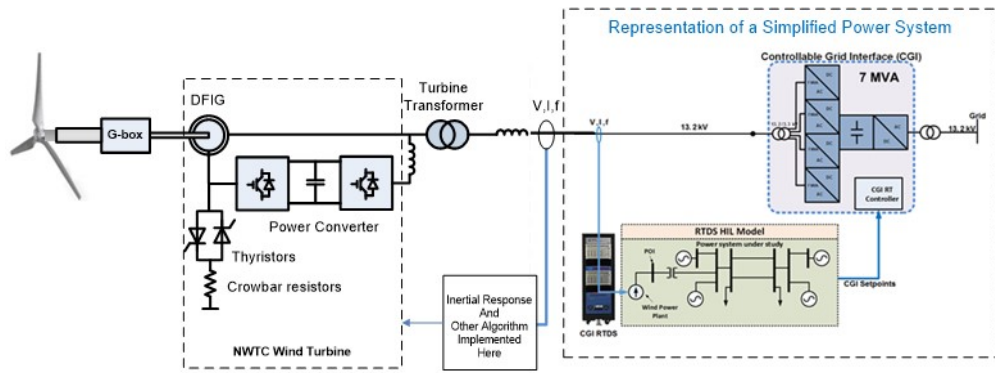


**Figure 34. Configuration of the PHIL simulation with the General Electric wind turbine**

## 7 Conclusions

To investigate the frequency support effects of variable-speed wind turbines, this work studies the controlled inertial response. The frequency stability of power systems deteriorates because of the decreased inertial response and undesirable primary frequency response in the context of the increased wind power penetration. Based on a series of simulation results obtained in the modeled nine-bus electric grid, various insights are provided in designing such kinds of inertial control methods for wind turbines.

We categorize the existing inertial control methods into two types: FBIC and SIC. Each presents different features when participating in power system frequency regulation. Wind turbines equipped with FBIC methods regulate the grid frequency with the other power sources in the grid by means of frequency measurement. In contrast, SIC methods command the power reference aggressively by following a predefined power reference in the speed-power plane. SIC methods tend to exploit the maximum frequency support capability of the turbine by understanding the overproduction capability; however, undesirable power injections might occur, which can cause a secondary frequency dip and frequency overshoot issues.

To solve the negative consequences in typical SIC methods, two improved SIC methods are adopted and implemented in this work: SAIC and TLIC. Further, the TLIC method is modified from a practical point of view, which makes it work under turbulent wind gusts. We start with a wind turbine mathematical model that facilitates the design of the inertial control methods. Later, a high-fidelity wind turbine simulator is used to further test the designed inertial control, emphasizing the turbine's response under turbulent wind conditions and the additional mechanical loads introduced by the inertial controls. After the comprehensive case studies, the designed inertial response controller blocks are ported to the CART3 SCADA system to control the real turbine, which takes advantage of the convenient code transformation between LabVIEW and Simulink.

The developed simulation platform facilitates the streamlined verification process of the proposed inertial controls. The inertial controls are completely evaluated and tuned in the secure simulation environment before operating in the field, and the results obtained in the CHIL test are similar to the results of the offline simulation and can be analyzed to further improve the inertial controls. The TLIC method generally shows more powerful frequency support than the FBIC method; however, the grid frequency profile might have a secondary frequency dip, and the overshoot is not as smooth as that in the FBIC. Finally, the inertial control methods are deployed in CART3, and it successfully responds to the emulated frequency decline in a modeled power system in RTDS when validated using CHIL techniques.

## References

1. E. Ela, V. Gevorgian, P. Fleming, Y. Zhang, M. Singh, E. Muljadi, A. Scholbrook, J. Aho, A. Buckspan, L. Pao, V. Singhvi, A. Tuohy, P. Pourbeik, D. Brooks, and N. Bhatt, *Active Power Controls from Wind Power: Bridging the Gaps* (Technical Report NREL/TP-5D00-60574) (Golden, CO: National Renewable Energy Laboratory, 2014).
2. P. W. Carlin, A. S. Laxson, and E. B. Muljadi, “The History and State of the Art of Variable-Speed Wind Turbine Technology,” *Wind Energy* 6:2 (2003): 129–159.
3. V. Gevorgian, Y. Zhang, and E. Ela, “Investigating the Impacts of Wind Generation Participation in Interconnection Frequency Response,” *IEEE Transactions on Sustainable Energy* 6:3 (2015): 1,004–1,012.
4. M. Altin, R. Teodorescu, B.B. Jensen, U.D. Annakkage, F. Iov, and P.C. Kjaer, “Methodology for Assessment of Inertial Response from Wind Power Plants,” *IEEE Power and Energy Society General Meeting Proceedings* (2012): 1–8.
5. J. Morren, J. Pierik, and S. W.H. De Haan, “Inertial Response of Variable Speed Wind Turbines,” *Electric Power Systems Research* 76:11 (2006): 980–987.
6. J. M. Mauricio, A. Marano, A. Gómez-Expósito, and J. Ramos, “Frequency Regulation Contribution through Variable-Speed Wind Energy Conversion Systems,” *IEEE Transactions on Power Systems* 24:1 (2009): 173–180.
7. N. R. Ullah, T. Thiringer, and D. Karlsson, “Temporary Primary Frequency Control Support by Variable Speed Wind Turbines—Potential and Applications,” *IEEE Transactions on Power Systems*, 23:2 (2008): 601–612.
8. S. El Itani El, U. D. Annakkage, and G. Joos, “Short-Term Frequency Support Utilizing Inertial Response of DFIG Wind Turbines,” *IEEE Power and Energy Society General Meeting* (2011): 1–8.
9. J. Lee, E. Muljadi, P. Sorensen, and Y. C. Kang, “Releasable Kinetic Energy-Based Inertial Control of a DFIG Wind Power Plant,” *IEEE Transactions on Sustainable Energy* 1 (2016): 279–288.
10. M. Kang, K. Kim, E. Muljadi, J.-W. Park, and Y. C. Kang, “Frequency Control Support of a Doubly-Fed Induction Generator Based on the Torque Limit,” *IEEE Transactions on Power Systems* 31:6 (2016): 4,575–4,583.
11. M. Kang, E. Muljadi, K. Hur, and Y. C. Kang, “Stable Adaptive Inertial Control of a Doubly-Fed Induction Generator,” *IEEE Transactions on Smart Grid* 7:6 (2016).
12. J. M. Jonkman and M. L. Buhl Jr., *FAST User’s Guide* (Technical Report NREL/EL-500-38230) (Golden, CO: National Renewable Energy Laboratory, 2005).

13. B. J. Jonkman, *TurbSim User's Guide: Version 1.50* (Technical Report NREL/TP-500-46198) (Golden, CO: National Renewable Energy Laboratory, 2009).
14. R. Schkoda, C. Fox, R. Hadidi, V. Gevorgian, R. Wallen, and S. Lambert, *Hardware-in-the-Loop Testing of Utility-Scale Wind Turbine Generators* (Technical Report NREL/TP-5000-64787) (Golden, CO: National Renewable Energy Laboratory 2016).
15. E. Muljadi, V. Gevorgian, M. Singh, and S. Santoso, "Understanding Inertial and Frequency Response of Wind Power Plants" (paper presented at the presented at the IEEE Symposium on Power Electronics and Machines in Wind Applications, Denver, Colorado, July 16–18, 2012).
16. B. Wu et al. *Power Conversion and Control of Wind Energy Systems* (New York: John Wiley & Sons, 2011).
17. M. Soliman, O.P. Malik, and D.T. Westwick, "Multiple Model Multiple-Input Multiple-Output Predictive Control for Variable Speed Variable Pitch Wind Energy Conversion Systems," *IET Renewable Power Generation* 5:2 (2011): 124–136.
18. E. Muljadi and C. P. Butterfield, "Pitch-Controlled Variable-Speed Wind Turbine Generation," *IEEE Transactions on Industry Applications* 37:1 (2001): 240–246.
19. P. A. Fleming, J. Aho, A. Buckspan, E. Ela, Y. Zhang, V. Gevorgian, A. Scholbrock, L. Pao, and R. Damiani, "Effects of Power Reserve Control on Wind Turbine Structural Loading," *Wind Energy* 19:3 (2015): 453–469.
20. Z. Wu, W. Gao, X. Wang, M. Kang, M. Hwang, Y. C. Kang, V. Gevorgian, and E. Muljadi, "Improved Inertial Control for Permanent Magnet Synchronous Generator Wind Turbine Generators," *IET Renewable Power Generation* 10:9 (2016): 1,366–1,373.
21. M. Hwang, E. Muljadi, J.-W. Park, P. Sorensen, and Y. C. Kang, "Dynamic Droop-Based Inertial Control of a Doubly-Fed Induction Generator," *IEEE Transactions on Sustainable Energy* 7:3 (2016): 924–933.
22. S. El Itani, U. D. Annakkage, and G. Joos, "Short-Term Frequency Support Utilizing Inertial Response of DFIG Wind Turbines," *IEEE Power and Energy Society General Meeting Proceedings* (2011): 1–8.
23. J. H. Eto, J. Undrill, P. Mackin, R. Daschmans, B. Williams, B. Haney, R. Hunt, J. Ellis, Ho. Illian, C. Martinez, M. O'Malley, K. Coughlin, K. H. LaCommare, *Use of Frequency Response Metrics to Assess the Planning and Operating Requirements for Reliable Integration of Variable Renewable Generation* (Technical Report LBNL-4142E) (Berkeley, CA: Lawrence Berkeley National Laboratory, 2011).
24. "WSCC 9-Bus System," The Illinois Center for a Smarter Electric Grid (ICSEG), Power Cases, accessed April 11, 2015, <http://publish.illinois.edu/smartergrid/wsc-9-bus-system/>.

25. J. M. Mauricio, A. Marano, A. Gómez-Expósito, and J. L. M. Ramos, “Frequency Regulation Contribution through Variable-Speed Wind Energy Conversion Systems,” *IEEE Transactions on Power Systems* 24:1 (2009): 173–180.
26. Z.-S. Zhang, Y-Z. Sun, J. Lin, and G-J. Li. “Coordinated Frequency Regulation by Doubly Fed Induction Generator-Based Wind Power Plants,” *IET Renewable Power Generation* 6:1 (2012): 38–47.
27. M. Steurer, F. Bogdan, W. Ren, M. Sloderbeck, and S. Woodruff, “Controller and Power Hardware-in-Loop Methods for Accelerating Renewable Energy Integration,” *IEEE Power Engineering Society General Meeting Proceedings* (2007).
28. B. Lundstrom, M. Shirazi, M. Coddington, and B. Kroposki, “An Advanced Platform for Development and Evaluation of Grid Interconnection Systems Using Hardware-in-the-Loop: Part III—Grid Interconnection System Evaluator,” *IEEE Green Technologies Conference Proceedings* (2013).
29. B. R. Lundstrom, “An Advanced Platform for Development and Evaluation of Grid Interconnection Systems Using Hardware-in-the-Loop” (Ph.D. diss., Colorado School of Mines, Arthur Lakes Library, 2007).
30. H. Li, M. Steurer, K.L. Shi, S. Woodruff, and D. Zhang, “Development of a Unified Design, Test, and Research Platform for Wind Energy Systems Based on Hardware-in-the-Loop Real-Time Simulation,” *IEEE Transactions on Industrial Electronics* 53:4 (2006): 1,144–1,151.
31. N. Ainsworth, A. Hariri, K. Prabakar, Annabelle Pratt, and Murali Baggu, “Modeling and Compensation Design for a Power Hardware in the Loop Simulation of an AC Distribution System” *North American Power Symposium Proceedings* (2016).